Title
Magnetic 3D Printing of Hexaferrite Material

Author
Ho, Max

Publication Date
2019

UNIVERSITY OF CALIFORNIA

Los Angeles

Magnetic 3D Printing of Hexaferrite Material

A dissertation submitted in partial satisfaction of the requirements for the degree

Doctor of Philosophy in Electrical and Computer Engineering

by

Max Ho

2019

ABSTRACT OF THE DISSERTATION

Magnetic 3D Printing of Hexaferrite Material

by

Max Ho

Doctor of Philosophy in Electrical and Computer Engineering

University of California, Los Angeles, 2019

Professor Robert Candler, Chair

The millimeter wave band, which corresponds to frequencies between 30 and 300 GHz, is heavily used in radar and satellite communications. For these applications, transmit-and-receive (T/R) modules are used to boost output power of the transmitted signal and establish noise figure, which is the degradation in the signal-to-noise ratio, of the system for receiving. Inside these modules, magnetic components such as circulators and isolators are critical to direct the flow of signals and allow both simultaneous transmission and reception using a single antenna. However, the inherently incompatible crystal structures of the ferrite-based magnetic components and their semiconductor-based electrical counterparts make integration of the two using conventional manufacturing methods difficult.

Additive manufacturing has emerged as a method of fabricating structures with complicated shapes. Recent efforts have begun incorporating magnetic materials with the method. One application for additive manufacturing of magnetic materials is miniaturization and integration of circulators. Using circulators in the 40-50 GHz range as a motivating application, requirements arise for the printed films, namely immunity to eddy currents, sufficient magnetization to act as a self-biasing field, and out-of-plane orientation of the self-biasing field. Based on these required properties, hexaferrite particles are selected for their strong magnetocrystalline anisotropy and low conductance. Due to their large internal anisotropy field, the particles of these materials tend to rotate to the field direction instead of changing magnetization direction under application of an external magnetic field, which is less than the anisotropy field. Methods of fabricating composites of hexaferrite particles and liquid polymer, SU8 were developed. Rotation of hexaferrite particles in polymer matrix and thus magnetic anisotropy has been demonstrated in the composite, which is subsequently cured to hold the physical position and orientation of the particles. The anisotropy of the self-biasing field provided by the films has been experimentally characterized via techniques like vibrating sample magnetometer and magnetic force microscopy, and a ferromagnetic resonance (FMR) frequency ~48 GHz has been observed via short waveguide method. We have also characterized the viscosity of the particle-laden polymer at different particle concentrations. 3D printing of this composite with poling will make direct printing of magnetic components that require out-of-plane and in-plane anisotropic magnetization possible.

The dissertation of Max Ho is approved.

Hossein Pirouz Kavehpour

Ankur M Mehta

Yuanxun Wang

Robert N. Candler, Committee Chair

University of California, Los Angeles

2019

Table of Contents

Acknowledgement

I would like to thank the Prof. Rob Candler for his continuous support and patience for my special situation. Throughout my path to the Ph.D. degree, I had to work as a half-time staff of UCLA to support my family financially. Without his permission, this situation would not have been possible. After my first research project lost its funding, Prof. Candler kept me motivated and looking for opportunities for me to finish my degree. For this act of kindness and generosity, he will always have my gratitude.

I would also like to thank Prof. James Rosenzweig for my initiation into the graduate school program. Without his initial research program of free-electron laser, I would have never started my Ph. D. program. My sincere thanks also goes to my manager, Dr. Wilson Lin. His tolerance and accommodation made my start into graduate school again after 10 years a possibility. I would also like to thank all the members of my dissertation committee: Prof. Yuanxun Ethan Wang, Prof. Pirouz Kavehpour, and Prof. Ankur Mehta. Their invaluable feedbacks and advice to my research made this thesis complete.

My colleagues in the Sensors and Technology Laboratory made my time in graduate school more pleasant. They helped and supported me throughout the journey in different ways. Thank you, Jimmy Wu, Sidhant Tiwari, Maggie Xiao, Ling Li, Yuan Dai, Siyuan Liu, and Ben Pound. I would also like to thank my collaborators: Dr. Rustu Umut Tok, Srinivas Prasad, and Aysan Rangchian.

Finally, I would like to thank PowderTech International for providing spherical strontium hexaferrite particles, and the UCLA Nanoelectronics Research Facility, the Center for High Frequency Electronics, and Nano and Pico Characterization Laboratory for use of their extensive fabrication facilities. This work was supported by DARPA under Award #W911NF-17-1-0101.

Vita

Max Ho

Education

University of California, Los Angeles: Ph.D. Electrical and Computer Engineering

University of Southern California: M.S. Materials Science and Engineering

University of California, Berkeley: B.S. Materials Science and Engineering

Employment

University of California, Los Angeles, California, March 2010 - Present, Senior Development Engineer in Nanoelectronics Research Facility

University of California, Los Angeles, California, September 2013 - July 2019, Graduate Student Researcher

Veeco Instruments, Santa Barbara, California, May 2004 - July 2008, Senior Application Engineer

Publications

Max Ho, Srinivas P. M. Nagaraja, Rustu Umut Tok, Aysan Rangchian, Pirouz Kavehpour, Yuanxun Ethan Wang, and Rob Candler, "Additive Manufacturing with Strontium Hexaferrite-Photoresist Composite," IEEE Trans. Magn., in review, 2019

Brian Naranjo, Max Ho, Phuc Hoang, Seth Putterman, Alessandra Valloni, and James B. Rosenzweig , "Photonic laser-driven accelerator for GALAXIE," AIP Conf. Proc. 1507, 488-92, 2012

Christian Froeck and Max Ho, "Characterization of photo masks by X3D AFM," 23rd European Mask and Lithography Conference, 2007

Anupam Madhukar, Siyuan Lu, Atul Konkar, Yi Zhang, and Max Ho, "Integrated semiconductor nanocrystal and epitaxical nanostructure systems: structural and optical behavior," Nano Lett., Vol. 5, No. 3, 479-82, 2005

Eui-Tae Kim, Zhonghui Chen, Max Ho, and Anupam Madhukar, "Tailoring mid- and long-wavelength dual response of InAs quantum-dot infrared photodetectors using In/sub x/Ga/sub 1-x/As capping layers," Journal of Vacuum Science & Technology B 20, 1188-91, 2002

Chapter 1: Introduction

Section 1.1: Millimeter Wave Communication

Millimeter wave, as the name suggests, is the band of electromagnetic spectrum with wavelength of millimeter. The frequency of this regime corresponds to 30 to 300 GHz. The oxygen and water molecules, which compose a significant portion of the atmosphere, interact and absorb the electromagnetic radiation strongly at 180 and 60 GHz, respectively [1], [2]. As a result, this frequency regime is ideal for satellite (which occurs in space) and covert communications (which welcomes long-range attenuation) on top of radar applications [1], [2]. For these applications, the communication systems used utilize radio frequency (RF) transmit and receive (T/R) modules. The main functions of these modules are boosting output power of the transmitted signal, establishing system noise figure, $NF(in\ dB) = 10 * \log[(\frac{S_{in}}{N_{in}})/(\frac{S_{out}}{N_{out}})]$, where S and N are signal and noise levels, respectively, for receiving, and providing beam steering control. The operation of the first two functions is illustrated in the block diagrams of a T/R module in Fig. 1. As shown in the figure, in transmit state, the module sends the signal and power from manifold to an antenna. Reflected signal and power from an antenna back to the amplifiers or down to the limiter could cause mixing signals and overloading. The same constraint applies to receive state of the module, signal and power from the antenna should not be sent back to the amplifier. Since weight and space saving is always welcome on satellites, a single antenna for both transmission and reception is desirable. A circulator would allow this to be achieved simultaneously in a T/R module by controlling the flow of transmitted and received signals so it only goes in one direction and preventing the reflections from the antenna to protect the electronic components [3]. For example, in a 3-port circulator, the signal would only go from Port 1 to Port 2 and not Port3, or from Port 2 to Port 3 and not Port 1, as shown in Fig. 2.

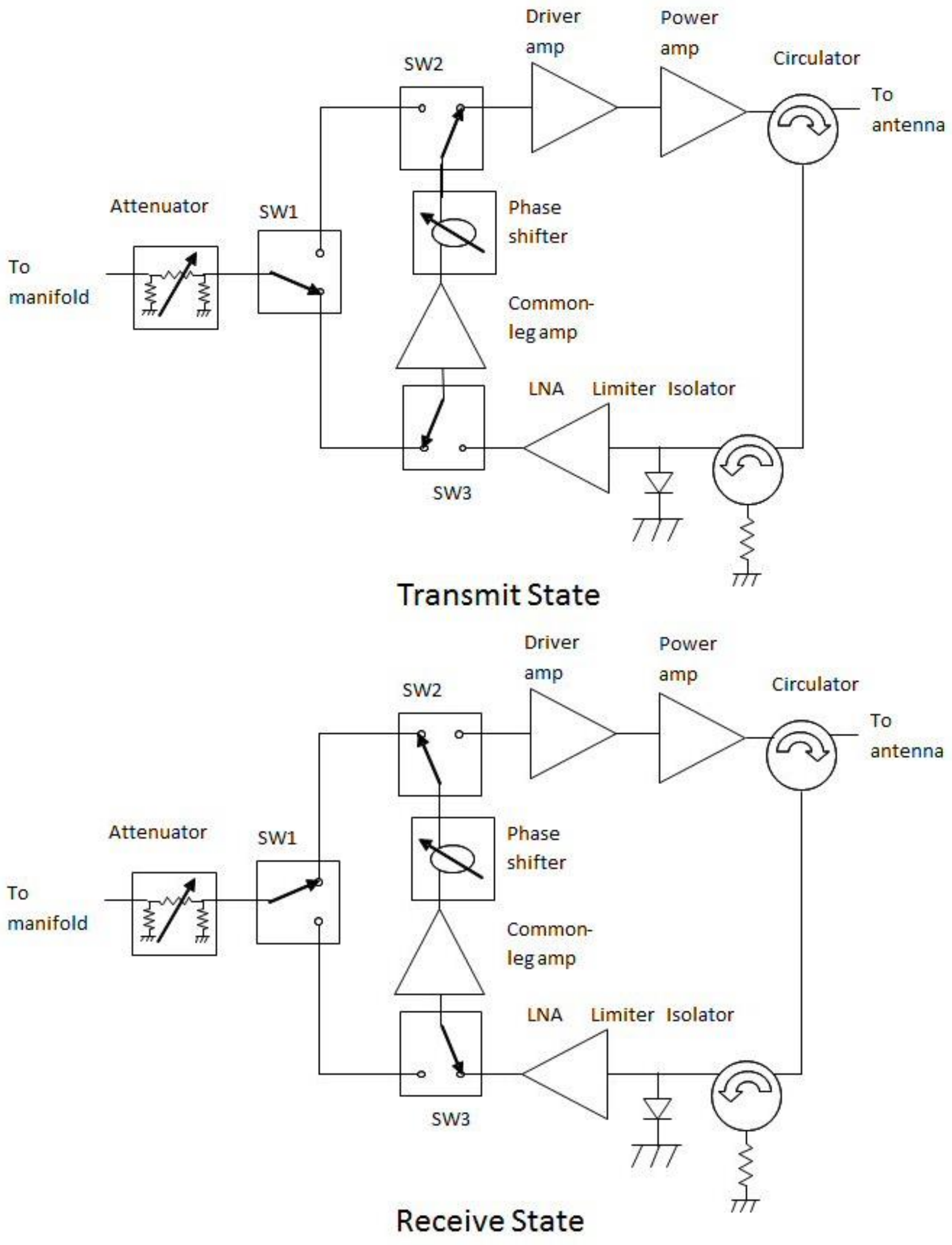

Figure 1 Operation of T/R Module [4]. *The circulator allows the single antenna to be shared between the transmit and receive states. The isolator (circulator with a grounded port in the block diagram) protects the antenna from the reflected signal. The limiter prevents damage to the low noise amplifier during transmit or whenever stray radiation is present, and the low-noise amplifier (LNA) sets the noise figure of the system, but all losses between the antenna and the LNA add to the overall noise figure and must be minimized. The phase shifter and often the attenuator are used in both transmit and receive paths. In this block diagram, an amplifier and the phase shifter are configured in the common-leg circuit (CLC). The attenuator is used to add an amplitude taper across the array, to reduce sidelobes. This is typically only done in receive state.*

An illustration of how a circulator functions (as a duplexer) is shown in the left side of Fig. 2. A RF isolator, on the other hand, ensures that the signal reflected from the receiving port never gets back to the source. This application is illustrated in the right side of Fig. 2. These passive components for millimeter-wave are usually made of ferrimagnetic materials, ferrites, or iron oxides, in particular. The magnetic materials possess unique physics and functionalities that are not available in their electrical counterparts. Unfortunately, ferrimagnetic materials, such as hexaferrites, used for these components possess crystal structures that are different and thus incompatible to those of electrical materials, which are often semiconductors. The cause of the incompatibility will be explained in the next chapter.

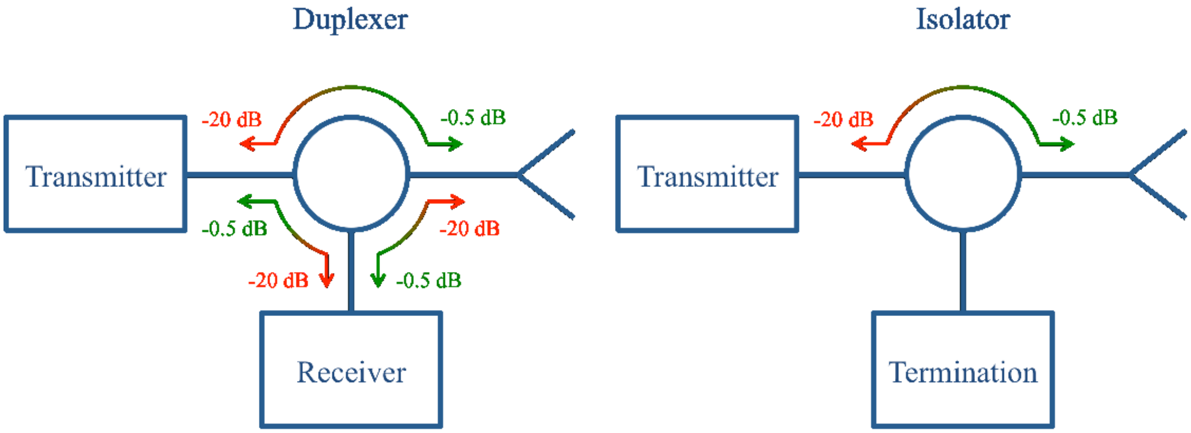

Figure 2 Schematics illustrate the functions of a circulator (duplexer) and an isolator [5]. *A circulator in a T/R module controls the flow of signals among the transmitter, antenna, and receiver. An isolator is a circulator with a grounded 3rd port and blocks reflected signal back to signal source.*

Section 1.2: Miniaturization and Integration of Magnetic with Electronic Components

Magnetic components are critical to the performance and operation of millimeter wave systems. The need for integrated magnetic components with semiconductors is demonstrated by these components used in the current RF T/R modules of communication and radar systems. These modules are assembled with monolithic microwave integrated circuits (MMICs) and large discrete (off-chip) magnetic components such as circulators, isolators, and inductors. A real example is shown in Fig. 3.

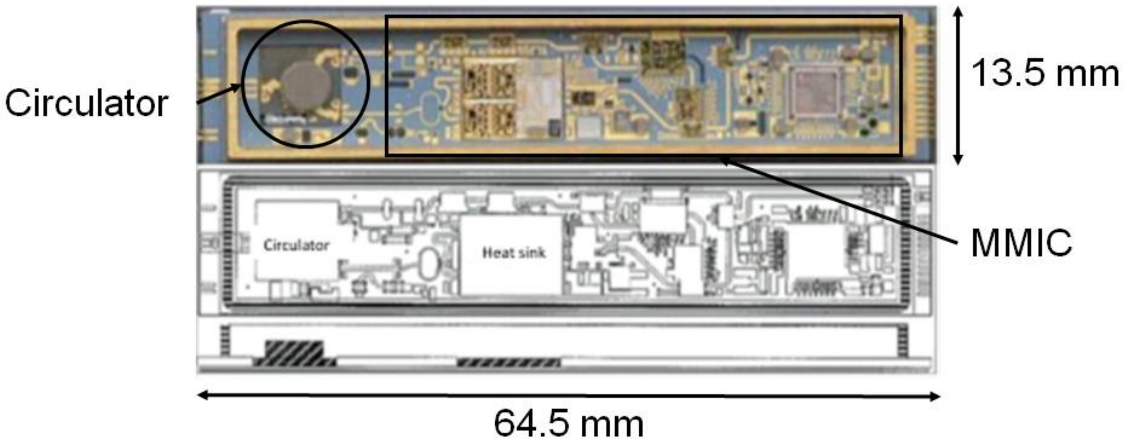

Figure 3 This is a real T/R module used in a Euro Typhoon Fighter's active phased array radar. On the left, this is just one component, a circulator, and on the right, you have quite a few Monolithic Microwave Integrated Circuits, or MMIC, such as low noise amplifiers, high power amplifiers, and complementary metal oxide semiconductor devices. The circulator, which is a magnetic component, is built separated from the MMICs. This type of components uses magnetic materials that exploit unique physics and functionality not available in semiconductor materials [4].

The black circle in the photo shows where a single circulator is, outside of MMICs, which filled most of the space left in the module as shown in the photo. High packing densities achievable on MMICs, the result of decades of investment in scalability and integration of elements such as transistors, resistors, and capacitors on semiconductor chips, are not achievable with current magnetic components. This type of components uses magnetic materials that exploit unique physics and functionality not available in semiconductor materials. It would be beneficial to monolithically integrate these magnetic components on semiconductor substrate to help reduce cost, size, weight, and power, or C-SWaP. However, there are some fundamental challenges that prevent monolithic integration and will be discussed in the following chapter. Fig. 4 shows the typical size dimension of just one circulator/isolator, and Fig. 5 shows the dimension of an entire MMIC. As such, critical magnetic components must be assembled off-chip, which adversely affects C-SWaP and constrains RF system design.

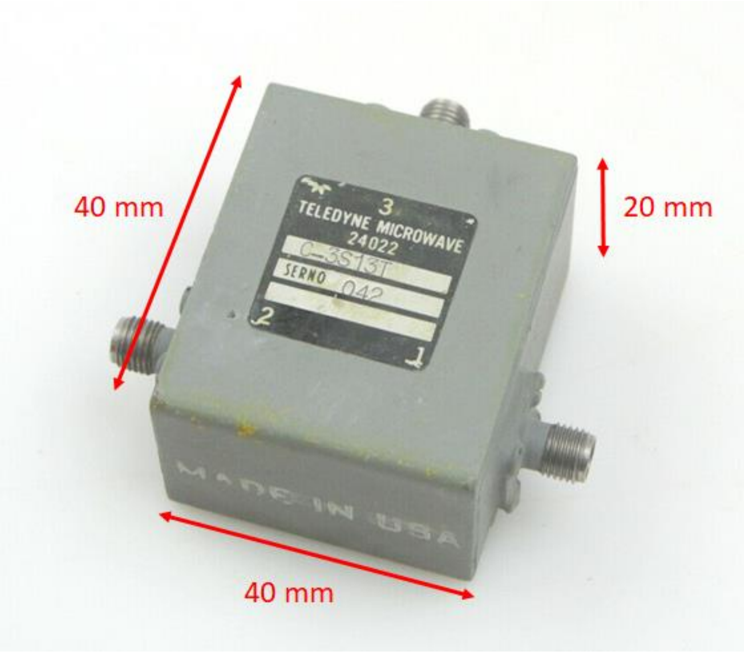

Figure 4 A Circulator dimension. Source: ebay.com

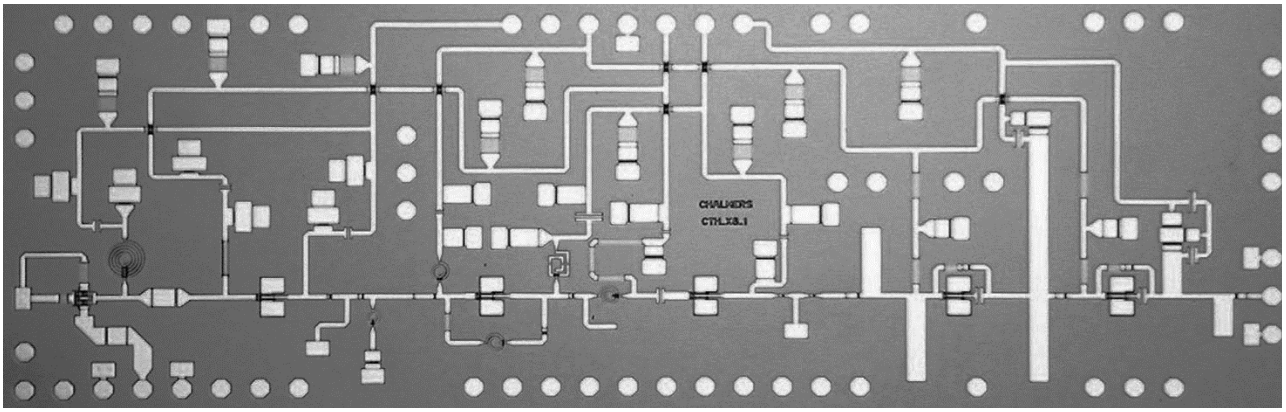

Figure 5 Photograph of the 8 pHEMT MMIC. The chip size is 5.0 x 1.6 mm [6]

Monolithically integrating high performance and self-biased microwave and millimeter wave magnetic components on semiconductor substrates can be accomplished by growing and patterning high-quality, uniform, thick, and temperature-stable magnetic films on standard semiconductor wafers while preserving the properties of both the magnetic films and the semiconductor circuitry. Depending on the application, the minimum film thickness required to access the magnetic properties of ferrite materials is on the order of 20 - 100 μm at mm-wave frequencies. Thicker films generally are more desirable as they allow for higher power handling and lower losses[7].

Section 1.3: 3D Printing

3D printing, a branch of additive manufacturing, has provided a methodology of fabricating structures with complicated shapes that has seen a surge in interest over the past decade; Fig. 6 shows an illustration of a typical 3D printer.

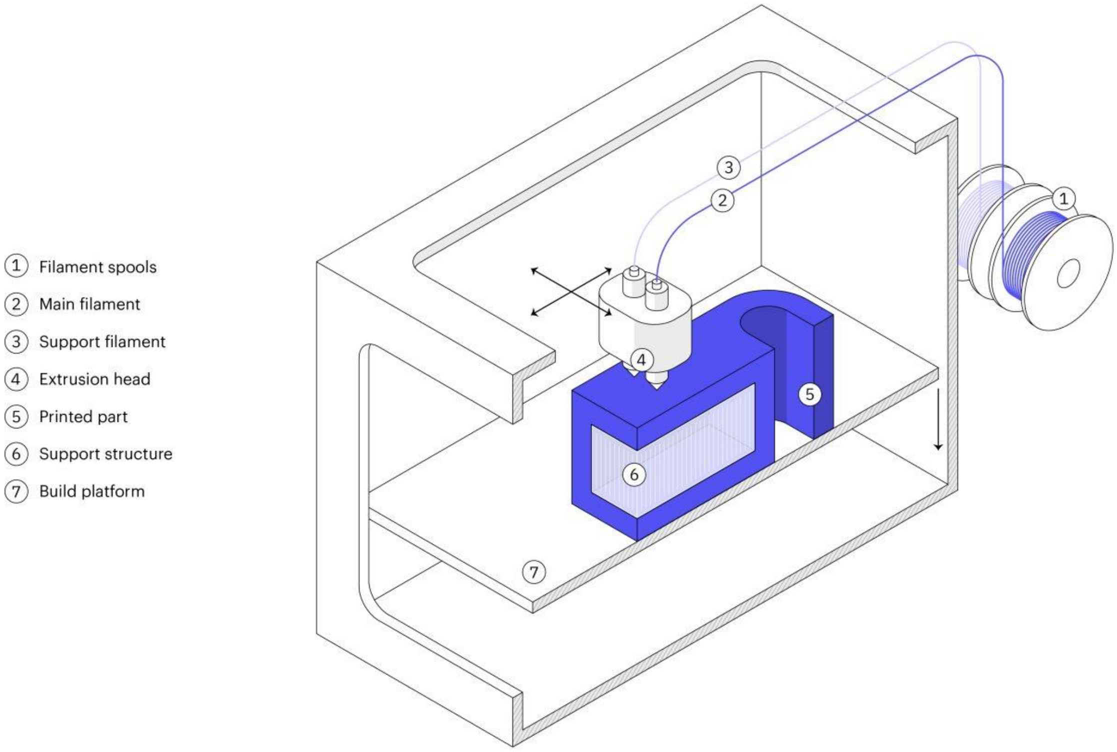

Figure 6 A schematic of FDM/FFF style of 3D Printer. Source: https://www.3dhubs.com/guides/3d-printing/#technologies

The material selection, however, is limited to those malleable at raised or room temperature for fused deposition modeling (FDM) or fused filament fabrication (FFF), the most common method of 3D printing [8] and shown in Fig. 6. The essential components of an FDM/FFF 3D printer are numbered and shown in the figure as well. While 3D printing has not overtaken traditional manufacturing and machining, it has shown its versatility in using different materials, including magnetic composites [9]–[11]. A class of smart materials known as magnetorheological elastomer [12]–[15], composites of polymer and magnetic materials, has been fabricated via traditional techniques and only recently by 3D printing. Prior research has demonstrated printing magnetic composite and poling it in the plane of printing [16], [17], where poling is the act of setting the magnetization of the composite in a desired direction. The same concept and technique can be applied to different magnetic materials, such as hexaferrite.

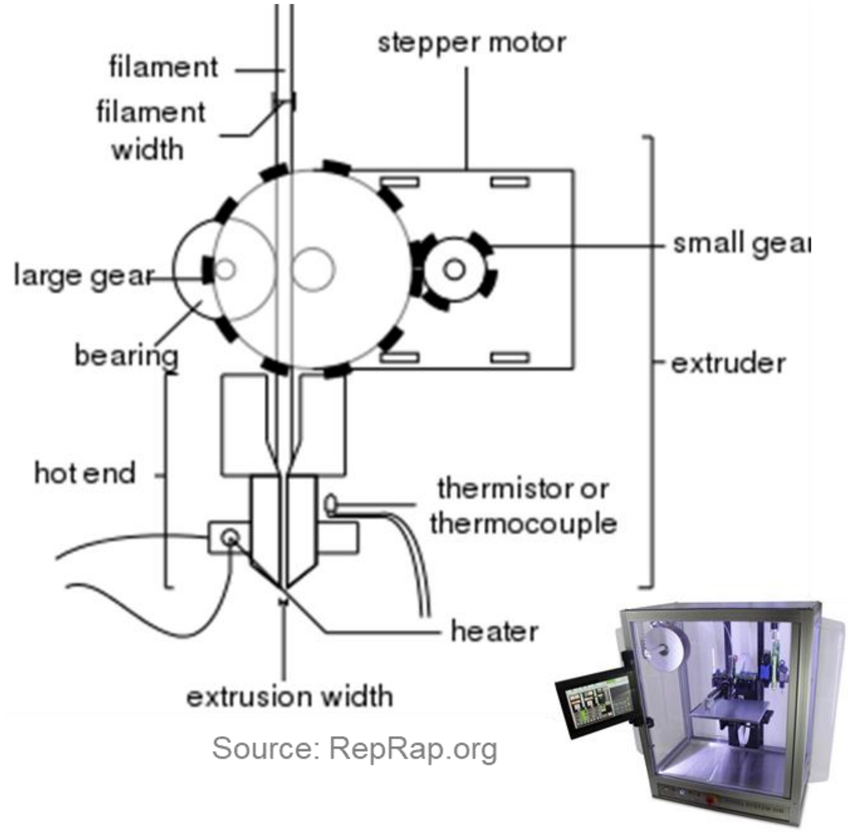

Source: RepRap.org

Figure 7 Schematic of FDM/FFF manufacturing. Source: Reprap.org and Hyrel3D.com

For this project, we select the FDM/FFF method for printing the materials for magnetic components. The schematic of the manufacturing method is shown in Fig. 7. The inset in the figure is the system used for this project, a Hyrel M30 printer. This method is picked for its flexibility in printing material; it allows printing of composite materials. While a solid, thermoplastic filament is shown in the figure, a liquid or gel type of composite can be used for deposition as well. The Hyrel M30 system has the advantage of modular design so different print heads can be applied if different print methods are needed.

In this body of work, printing a composite of SU8 photoresist and strontium hexaferrite (SrFe12O19) and poling it out of plane with respect to the printing platform is demonstrated. This technique opens the possibility of fabricating magnetic components, such as circulator and inductors; it also makes integration with electrical components much easier and at lower cost because it eliminates the need for the high temperature processing and photolithography that are associated with traditional approaches. A different composite, using thermoplastic polymer and hexaferrite particles, was also tried and tested in the preliminary phase of this study; however, the composite could not be poled sufficiently. This failed effort can still be applied for different applications so the procedure and results are shown in Appendix.

Chapter 2: Background and Theory

Section 2.1: Hexaferrites

Hexaferrite materials possess low conductivity and self-bias, which make them suitable for millimeter wave devices [18], [19]. Due to recent demand in telecommunication and wireless communication, there is a renewed interest in making magnetic devices out of this type of material [20], [21]. These hexaferrites also possess high internal fields to enable self-bias, thus eliminating the need for large and bulky external bias magnets. The strength of the internal field, which comes from magnetocrystalline anisotropy (MCA), can be tuned through selective cation substitutions. In addition, the high electrical resistance of hexaferrites suppresses eddy currents and makes the materials suitable for high frequency applications. These properties make hexaferrite ideal for making circulator and isolators. While this work focuses on the frequency range of 40 to 50GHz, there are other hexaferrites that are suitable for other ranges of millimeter wave spectrum.

Unfortunately, the hexagonal-type crystal structure of hexaferrites makes them inherently incompatible with the cubic lattices of standard semiconductor substrates. The difference is illustrated in Fig. 8. The commonly used semiconductor substrates such as silicon and gallium arsenide have a face-centered cubic lattice, which is very different from that of hexagonal lattice of hexaferrite materials such as strontium hexaferrites and barium hexaferrites. When conventional epitaxial methods are used to grow hexaferrite film on top of the cubic lattice semiconductor, the mismatch will cause dislocations and amorphous structure instead of the hexagonal crystal structure. As a result, the film would usually lose magnetic properties [22]–[26]. High-temperature annealing is needed to make the film magnetic again; however, the annealing process makes it incompatible with the other steps used in semiconductor processing. Another issue that arises from the thin-film deposition is that the thickness of the film is the demagnetization associated with the geometry. The details of demagnetization is further explained in the next section. Basically, due to its aspect ratio of a thin-film between its height and other two dimensions, the demagnetization factor is high so the out-of-plane remanent magnetization is low [27]. Therefore, the film thickness has to be large enough to mitigate the demagnetization. Chen and Harris did a great review on the past efforts to grow hexaferrite film with out-of-plane magnetization [28].

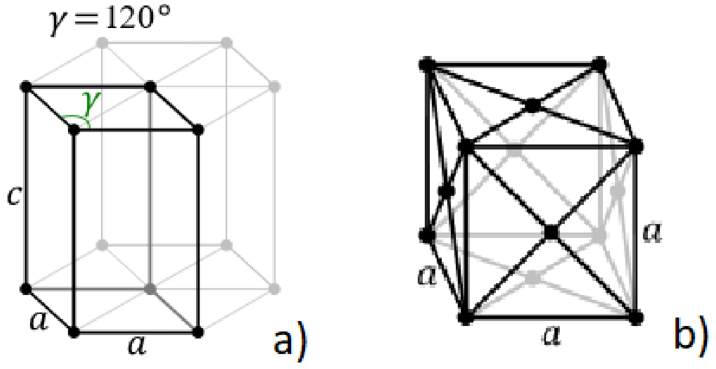

Figure 8 Different 3D lattices of hexaferrite, which is hexagonal a), and typical semiconductor material like silicon and GaAs, which is face-centered cubic b)[29]

This incompatibility has led to development of many novel techniques to deposit thick film [28], [30]. Unfortunately, most of the techniques are limited by selection of substrate, film thickness, or processing such as high temperature curing, which makes direct integration with MMICs difficult. Using a composite of hexaferrite particles and photoresist can overcome the obstacles mentioned. Though this technique has been used in prior work [31]–[33], applying this composite with 3D printing makes it even more versatile than the traditional spin-on and photolithography method. The ferrimagnetic materials of interest, hexaferrites, are iron oxide and characterized by their hexagonal crystal structure. These materials were first developed and studied by the workers at Philips Laboratories [34]–[37]. This type of ferrite always contain a divalent cation of rare-earth element(s). There are many types of hexaferrites, characterized by their crystal structures. Due to the limit of scope, this study focuses on the M-type hexaferrite. The crystal structure of this type is shown in the Fig. 9. The chemical formula of M-type hexaferrite is $MeFe_{12}O_{19}$, where Me is the rare-earth element; Me is either barium or strontium in this study. Barium hexaferrite particles are imaged in SEM, shown in Fig. 10, to show the usual shapes of these particles.

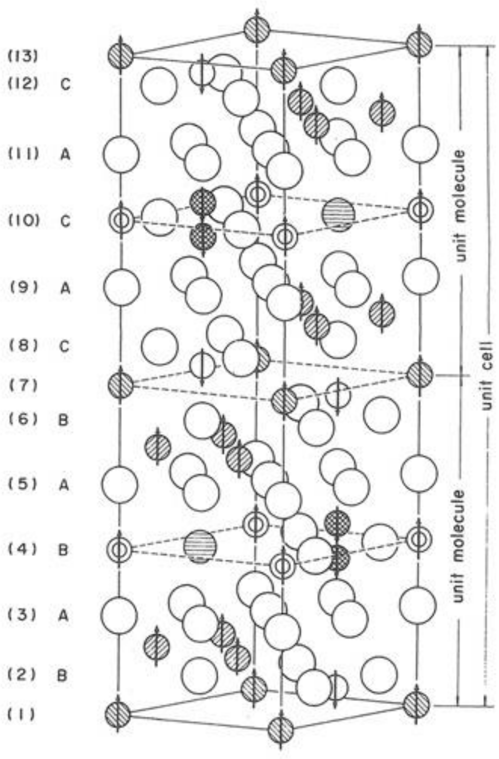

Figure 9 The crystal structure of M-type of hexaferrite [38]

The special material property, MCA or magnetocrystalline anisotropy, means that the magnetization has a preferred direction associated with the crystal structure. The cause of this characteristic is attributed to the large barium or strontium ion presence in the crystal structure [39]. The uniaxial nature of the anisotropy is attributed to the c-axis that is perpendicular to the basal plane, which has a six-fold symmetry. MCA also makes the material self-biased. Self-biasing in magnetics means that there is a non-zero magnetization in the material without an external magnetic field.

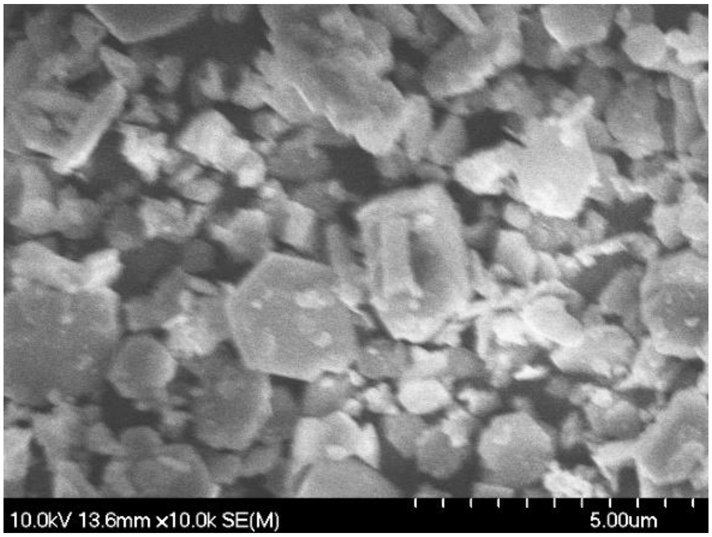

Figure 10 SEM image of BaM particles, which have the general shape of hexagonal disc

Section 2.2: Circulators/Isolators

The concept of a microwave circulator was first introduced by Chait and Curry, who explained the concept clearly in their paper in 1959 [40]. Pozar gave an analytical and mathematical treatment of the principles in Chapter 9 of his book [41]. The key parts will be reiterated here. There are two types of constructions for circulators; both of them have a three-fold symmetry. Three waveguides meet and form a symmetrical Y-shape junction, where every waveguide is 120° from another. One type of circulator has three rectangular waveguides meeting at the junction with a ferrite post in the center of the junction as illustrated in Fig. 11. In the other type of construction, a ferrite circular disc resides on each side of the junction of the waveguides, usually in the form of strips in this case as illustrated in Fig. 12 [42].

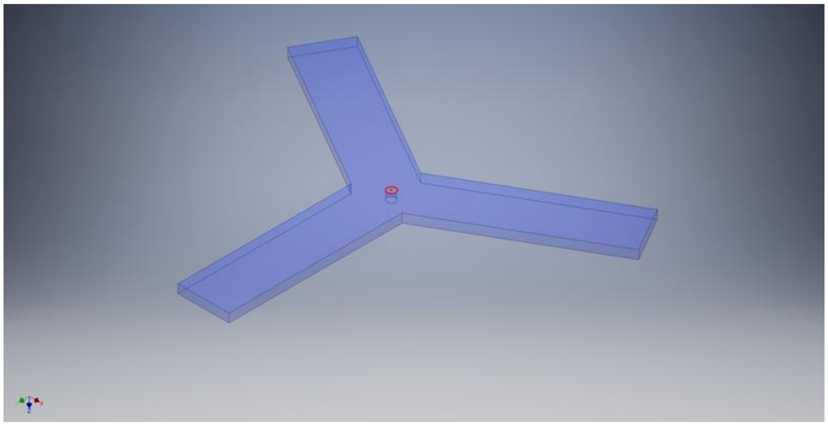

Figure 11 Schematic of a ferrite post circulator; the center circle in red shows where the post is

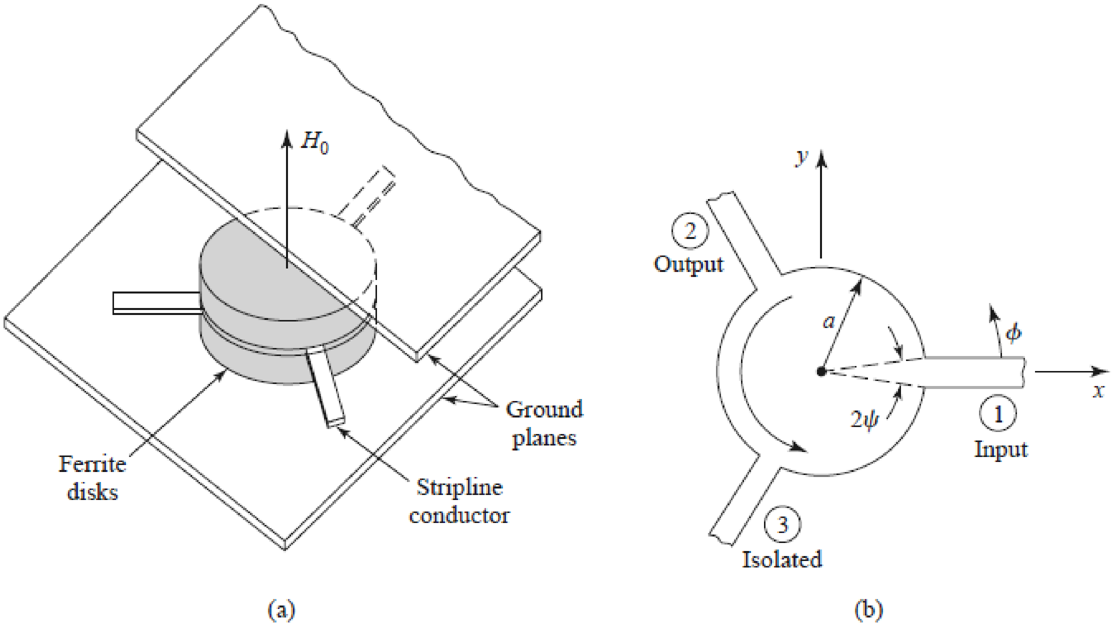

Figure 12 a) the cross-section of a circulator with ferrite discs and b) its geometry [41]

Both types also rely on the presence of an asymmetrical magnetic field provided by the magnetized ferrite. From the perspective of an electromagnetic wave traveling toward the junction, the geometry would be identical from every port. However, the field distribution of the wave inside the waveguide is not symmetrical, as illustrated in Fig. 13. The H fields are polarized elliptically in planes either along or normal to the traveling direction, and is of opposite orientation in either side of the waveguide. Since permeability is a tensor and thus depends on the orientation, the wave will experience asymmetry as it passes through the external magnetic field from the magnetic ferrite. A mathematical analysis of the structure that explains how a circulator works is iterated below.

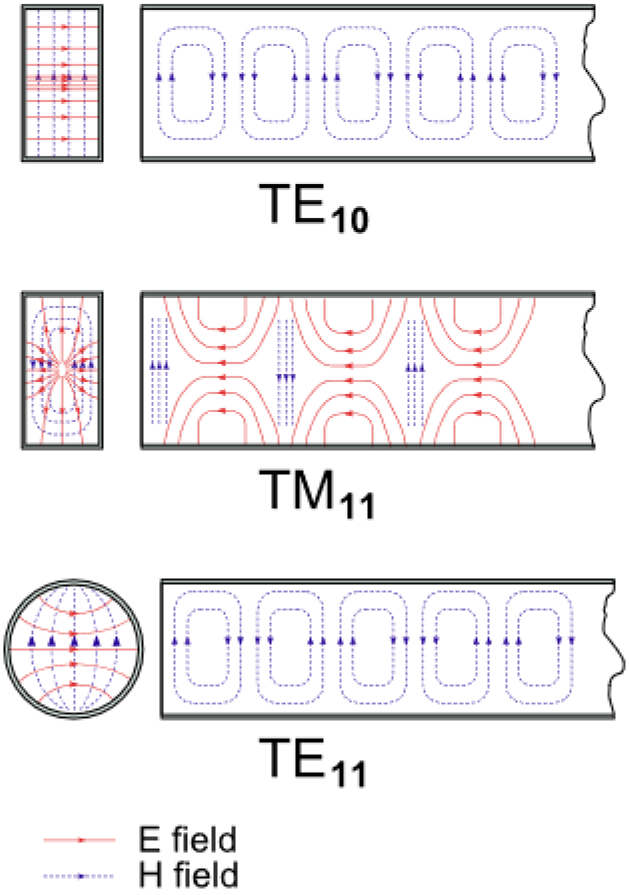

Figure 13 Typical propagation modes in waveguides, where TE and TM refer to transverse electric and transverse magnetic modes, respectively [43]

From Maxwell's Equations, it is known that $\vec{B} = [\mu]\vec{H}$, where the permeability, $[\mu]$, is a tensor. Using the coordinate system shows in Fig. 12 b), the equation can be written in cylindrical coordinates. Now the equation is in matrix form:

$$\begin{bmatrix} B_\rho \\ B_\rho \\ B_z \end{bmatrix} = [\mu] \begin{bmatrix} H_\rho \\ H_\rho \\ H_z \end{bmatrix} \quad \textit{(2- 1)}$$

The permeability tensor is:

$$[\mu] = \mu_0[U] + [\chi] = \begin{vmatrix} \mu & j\kappa & 0 \\ -j\kappa & \mu & 0 \\ 0 & 0 & \mu_0 \end{vmatrix} \quad \textit{(2- 2)}$$

μ_0 is the permeability of free space and Eqn. 2-2 conforms to the H-field direction shown in Fig. 12b), in the z-direction. With $\frac{\partial}{\partial z} = 0$, Maxwell's curl equation in cylindrical coordinates is now in the following form:

$$\frac{1}{\rho}\frac{\partial E_z}{\partial \phi} = -j\omega(\mu H_\rho + j\kappa H_\phi) \quad \textit{(2- 3)}$$

$$-\frac{\partial E_z}{\partial \rho} = -j\omega(-j\kappa H_\rho + \mu H_\phi) \quad \textit{(2- 4)}$$

$$\frac{1}{\rho}[\partial\left(\frac{\rho H_\phi}{\partial \rho} - \frac{\partial H_\rho}{\partial \phi}\right) = j\omega\epsilon E_z \quad \textit{(2- 5)}$$

The solution for H_ρ and H_ϕ in terms of E_z from Eqn. 2-4 and 2-5 is:

$$H_\rho = \frac{jY}{k\mu}\left(\frac{\mu}{\rho}\frac{\partial E_z}{\partial \phi} + j\kappa\frac{\partial E_z}{\partial \rho}\right) \quad \textit{(2- 6)}$$

$$H_\phi = -\frac{jY}{k\mu}\left(-\frac{j\kappa}{\rho}\frac{\partial E_z}{\partial \phi} + \frac{\mu \partial E_z}{\partial \rho}\right) \quad \textit{(2- 7)}$$

$$k^2 = \frac{\omega^2\epsilon(\mu^2 - \kappa^2)}{\mu} = \omega^2\epsilon\mu_e \quad \textit{(2- 8)}$$

$$Y = \sqrt{\epsilon/\mu_e} \quad \textit{(2- 9)}$$

Substituting the H_ρ and H_ϕ in Eqn. 2-5 with Eqn. 2-6 and 2-7, the E_z gets a wave equation:

$$\frac{\partial^2 E_z}{\partial \rho^2} + \frac{1}{\rho}\frac{\partial E_z}{\partial \rho} + \frac{1}{\rho^2}\frac{\partial^2 E_z}{\partial \phi^2} + k^2 E_z = 0 \qquad (2\text{-}10)$$

The general solution of this wave equation (Eqn. 2-10) can be in the following form:

$$E_{zn} = \left[A_{+n} e^{jn\phi} + A_{-n} e^{-jn\phi}\right] J_n(k\rho) \qquad (2\text{-}11)$$

$$H_{\phi n} == jY\left\{A_{+n} e^{jn\phi}\left[J_n'(k\rho) + \frac{n\kappa}{k\rho\mu} J_n(k\rho)\right] + A_{-n} e^{-jn\phi}\left[J_n'(k\rho) - \frac{n\kappa}{k\rho\mu} J_n(k\rho)\right]\right\} \qquad (2\text{-}12)$$

where J_n and Y_n are ordinary Bessel functions of the first and second kind, respectively. By enforcing the boundary condition that $H_\phi = 0$ at $\rho = a$, where a is the radius of the ferrite disc, the resonant modes can be calculated. Due to the presence of the H field from the magnetic ferrite, there are two possible resonant modes for each value of n, as associated with either $e^{jn\phi}$ or $e^{-jn\phi}$. For $n = 1$, the resonance condition for the two modes is:

$$\frac{\kappa}{\mu x} J_1(x) \pm J'_1(x) = 0,\ x = ka \qquad (2\text{-}13)$$

Eqn. 2-13 shows the nonreciprocal property of the circulator because changing the sign of κ leads to the other root and propagation in the opposite orientation in ϕ.

Using x_+ and x_- as the two roots of Eqn. 2-13, the two resonant frequencies for $n = 1$ can be written as:

$$\omega_\pm = \frac{x_\pm}{a\sqrt{\epsilon\mu_e}} \qquad (2\text{-}14)$$

The approximate result for $\omega_\pm$ can be calculated assuming that κ/μ is small. Using a Taylor series about x_0 for the 1st two terms in Eqn. 2-13, the results are:

$$J_1(x) \approx J_1(x_0) + (x - x_0)J_1'(x_0) = J_1(x_0) \qquad (2\text{-}15)$$

$$J'_1(x) \approx J'_1(x_0) + (x - x_0)J''_1(x_0) = -(x - x_0)\left(1 - \frac{1}{x_0^2}\right)J_1(x_0) \quad \textit{(2- 16)}$$

Using these two approximation to substitute the functions in Eqn. 2-13 will simplify it to:

$$\frac{\kappa}{\mu x_0} \mp (x_\pm - x_0)\left(1 - \frac{1}{x_0^2}\right) = 0,\ x_\pm \approx x_0\left(1 \pm 0.418\frac{\kappa}{\mu}\right), x_0 = 1.841 \quad \textit{(2- 17)}$$

From Eqn. 2-17, we can get the two resonant frequencies in Eqn 2-14. The superposition of these two modes can be used to design a circulator; the amplitudes of the modes provide coupling from one port to another and cancellation to the other.

Section 2.3: Poling

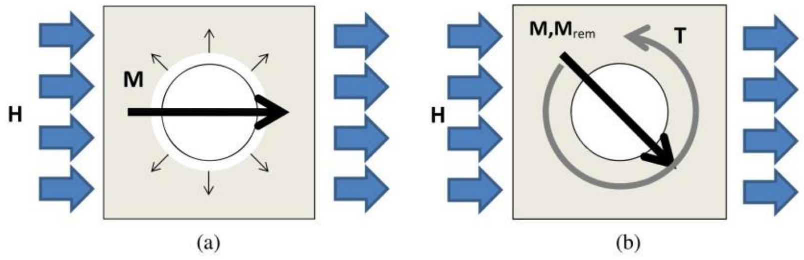

(a)
(b)

Figure 14 Soft magnetic material (left), which changes its magnetization direction to the direction of the external magnetic field, H, vs hexaferrite (right), which rotates itself physically so the magnetization direction is in the direction of the external magnetic field [12]

Some millimeter wave devices, such as isolator and circulators, require magnetic bias fields; their presence makes a microwave signal for a given polarization propagate through the magnetic material differently in different directions [41], as detailed in the last section. In order to achieve this goal, the magnetic material needs to be poled. To pole means to align the magnetization of the material in one direction; this is usually achieved by using an external magnetic field to force the magnetization in the direction of the field. By aligning the magnetization, the remanence of the material also increases.

Because of the strong MCA in hexaferrites, poling them can be quite different from poling soft magnetic materials. As shown in Fig. 14, instead of changing the magnetization direction in the particle when it experiences an external magnetic field, it is may be easier to change the physical orientation of the entire crystal. A single-domain, hexaferrite particle experiences a torque that equals to the cross product of the magnetization and magnetic flux from the applied field. The torque is calculated by this equation,

$$\vec{T} = \vec{m} \times \vec{B} = \mu_0 \vec{m} \times \vec{H}$$

The $\vec{m}$ in the equation is the magnetic moment of the particle, $\vec{B}$ and $\vec{H}$ are the applied magnetic-flux and field, respectively, and μ_0 is the permeability of free space. However, there are additional forces and torques acting on a particle inside a fluid beyond the presence of a magnetic field. If the motion of a particle is separated into translation and rotation, the rotation of the particle can be described in the following equation:

$$I \frac{d^2\theta}{dt^2} = \sum \tau^i$$

The *I* in the equation is the rotational inertia of the particle, θ is the angle of rotation made by the particle, and τ is the different torques acting on the particle. For a hexaferrite particle in fluid, the equation above can be written as the following:

$$I \frac{d^2\theta}{dt^2} = m * B * \sin\theta + L \frac{d\theta}{dt} \qquad (2\text{- }18)$$

The *m* in the Eqn. 2-18 is the magnetic moment of the particle, and *B* is the magnetic flux from the applied field. The *L* is hydrodynamic constant for drag of the particle. This rotation of a particle is illustrated in Fig. 15. For a sphere, the value of the constant is: $L = 8\pi\eta r^3$. η is the viscosity of the fluid in which the particle rotates. However, as shown in Fig. 10, the shape of the hexaferrite particles are normally far from spherical and closer to ellipsoid. The *L* value, therefore, needs adjustment. For an ellipsoid, $L = 8\pi\eta a^3/\mathrm{F}(D)$, where *a* is the half the distance of the short axis of the ellipsoid, as sown in Fig. 16, and *D* is the ratio between the distances of short axis and long axis, *b*. $\mathrm{F}(D) = 3D(-2D\sqrt{D^2+1} + (1 - 2D^2) ln \, {}^{D - \sqrt{D^2-1}}\!/\!{}_{D + \sqrt{D^2-1}})/(4(D^2-1)(D^2+1)\sqrt{D^2-1})$. This geometric form factor is analyzed by George B. Jeffery [44]. For reference, the volume of an ellipsoid is $V = \left(\frac{4}{3}\right)\pi a^3 D$.

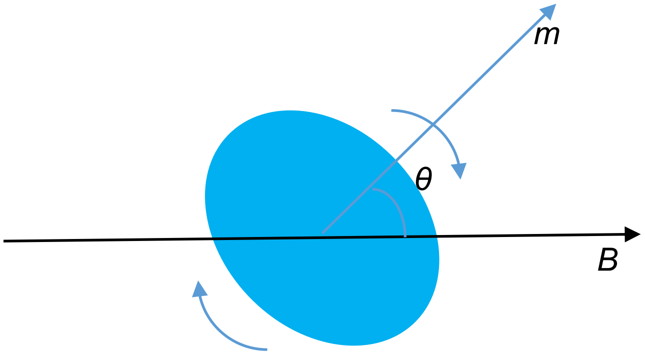

Figure 15 Rotation of ellipsoidal particle in fluid under an applied magnetic field. m is the magnetization of the ellipsoid, B is the magnetic flux from an external magnetic field, and θ is the angle between them.

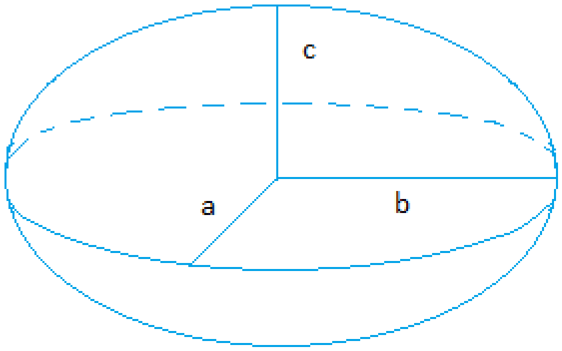

Figure 16 Ellipsoid and geometric factor. Axes a and c are the minor, or shorter, axes of the ellipsoid. Axis b is the major, or longer axes of the ellipsoid. D is b/a if a = c.

For simplicity of the solution to Eqn. 2-18, it is easier to assume that the angular acceleration, or $\frac{d^2\theta}{dt^2}$ is 0. Now eq. 2-18 becomes a simpler equation:

$$L\frac{d\theta}{dt} = m * B * \sin\theta \qquad \text{(2- 19).}$$

This is not an unrealistic assumption, similar mathematical treatment is done by Kimura *et al.* [45], and good agreement is reached between the assumption and actual rotation observed. An important feature of Eqn. 2-19 is that the volume or size of the particle does not matter, only the aspect ratio of the axes of the ellipsoid affect the rotation. This is because *L* = $8\pi\eta a^3$/F(D), and the unit of η is Pa*s, which can also be written as $\frac{J}{m^3} * s$, and the a^3 has units of m^3, which reduces the units of *L* to *J**s*. Since $m * B * \sin\theta$ has unit of torque, *N*m or J, and L* $\frac{d\theta}{dt}$ also has units of $J * s * s^{-1} = J$, the equation is shown to be independent of volume.

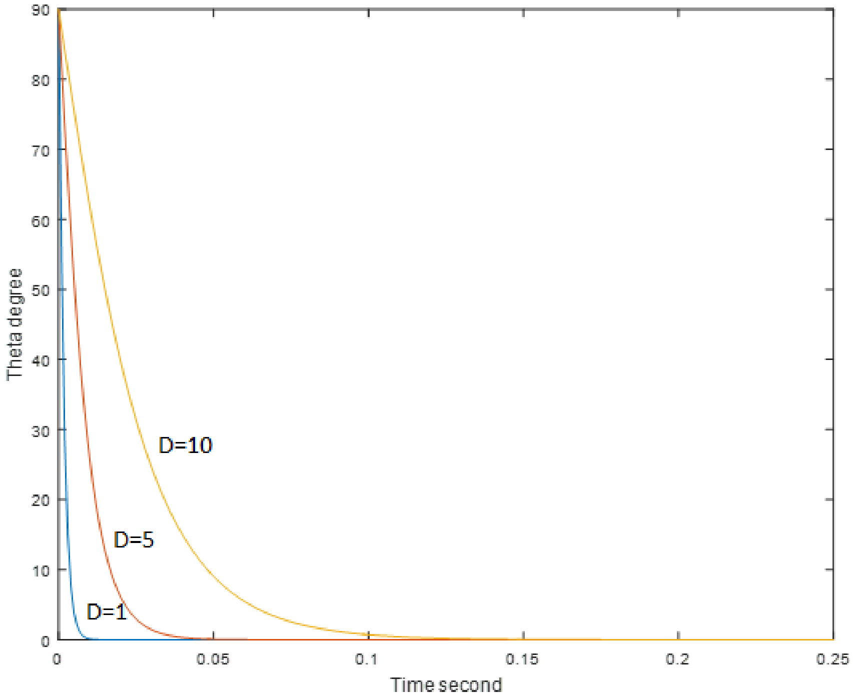

Figure 17 Time of rotation for different aspect ratio D. The viscosity is that of SU8 2000.5, and the external field used is 0.04 T. As the graphs show, the higher the D value (aspect ratio) is, the longer it takes for the particles to rotate into the direction of the external magnetic field

Solving Eqn. 2-19 with viscosity of 2.66 Pa*s, which is that of SU8 2000.5 and an external field of 0.04 T, the rotation from 90 degree to the field direction to that of parallel to the field is plotted against time. As the results are shown in Fig. 17, even when the aspect ratio is as large as D = 10, the rotation time under such conditions is only about 0.2 second. However, in the initial experiments, it is found that this is not the case. There are a number of causes; the first one is the demagnetization. Due to their disc-like shapes, the particles have high aspect ratio, which leads to high value in demagnetizing factor, as shown in the table in Fig. 18.

Dimensional Ratio (length/diameter)	Rod	Prolate Ellipsoid	Oblate Ellipsoid
0	1.0	1.0	1.0
1	0.27	0.3333	0.3333
2	0.14	0.1735	0.2364
5	0.040	0.0558	0.1248
10	0.0172	0.0203	0.0696
20	0.00617	0.00675	0.0369
50	0.00129	0.00144	0.01532
100	0.00036	0.000430	0.00776
200	0.000090	0.000125	0.00390
500	0.000014	0.0000236	0.001567
1000	0.0000036	0.0000066	0.000784
2000	0.0000009	0.0000019	0.000392

Figure 18 Demagnetization Factor, N/4π, for rods and ellipsoids magnetized parallel to long axis [46]

High demagnetizing factor leads to low effective magnetization in the particles. The high aspect ratio of the particles also leads to another problem, which is already mentioned and shown, and that is the increase in rotational drag. As it is shown in Fig. 17, the higher the aspect ratio, the longer it takes to rotate a particle under an external magnetic field. The common solution to these two causes is to use spherical hexaferrite particles. PowderTech International Inc., a company that specializes ferrite powder, provided us samples of spherical strontium hexaferrite.

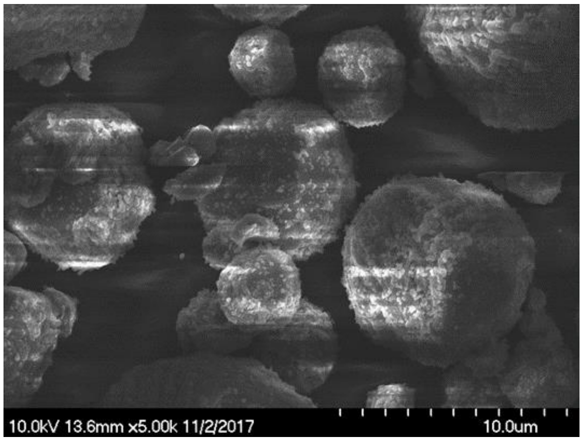

Figure 19 Spherical strontium hexaferrite particles

The SEM image of these particles in Fig. 19 shows that the shape is much more spherical than those used earlier. A less obvious cause, particle-particle interaction, shows up later while making the strontium hexaferrite-polymer composite. This model of particle rotation does not take into account of the force among particles. For particles that are non-polar, the interaction force among them is usually very short-range and weak; however, for hexaferrite particles, the force is much larger and longer range. In order for this model to stay valid, therefore, the distances between particles must stay large enough. In other words, the concentration must stay low, much lower than 25%, which was the concentration for negligible self-interaction between particles [47]–[49].

Section 2.3: Magnetic Composite

Composites of polymer matrix with hard magnetic particles inside have been studied as a class of materials for different applications. In earlier studies, the motivation of this type of composite was simply to improve manufacturability so high-temperature processing like sintering can be avoided [50], [51]. Later on, this concept is extended to build so-called smart materials [12], [52] so it can deflect and therefore actuate under external magnetic fields. For these applications, the composite is fabricated by mixing the magnetic particles inside liquid polymer. The mixture, or slurry, is then casted and then cured, either with or without an external magnetic field present during the curing process. Since the mixture is poured into a mold to form the desired shape, the freedom to create complex 3D shape is limited to the capability to make the molds. However, these studies focus on the mechanical response of the composite to the external magnetic stimuli [53]. The magnetic composites used for electronic purpose are often associated with photolithography so the polymer matrix used is often photosensitive and requires a mask for patterning [21], [31], [54]. In one study [21], a monolithically integrated circulator is built, as shown in Fig. 20. The circulator was measured and showed non-reciprocity.

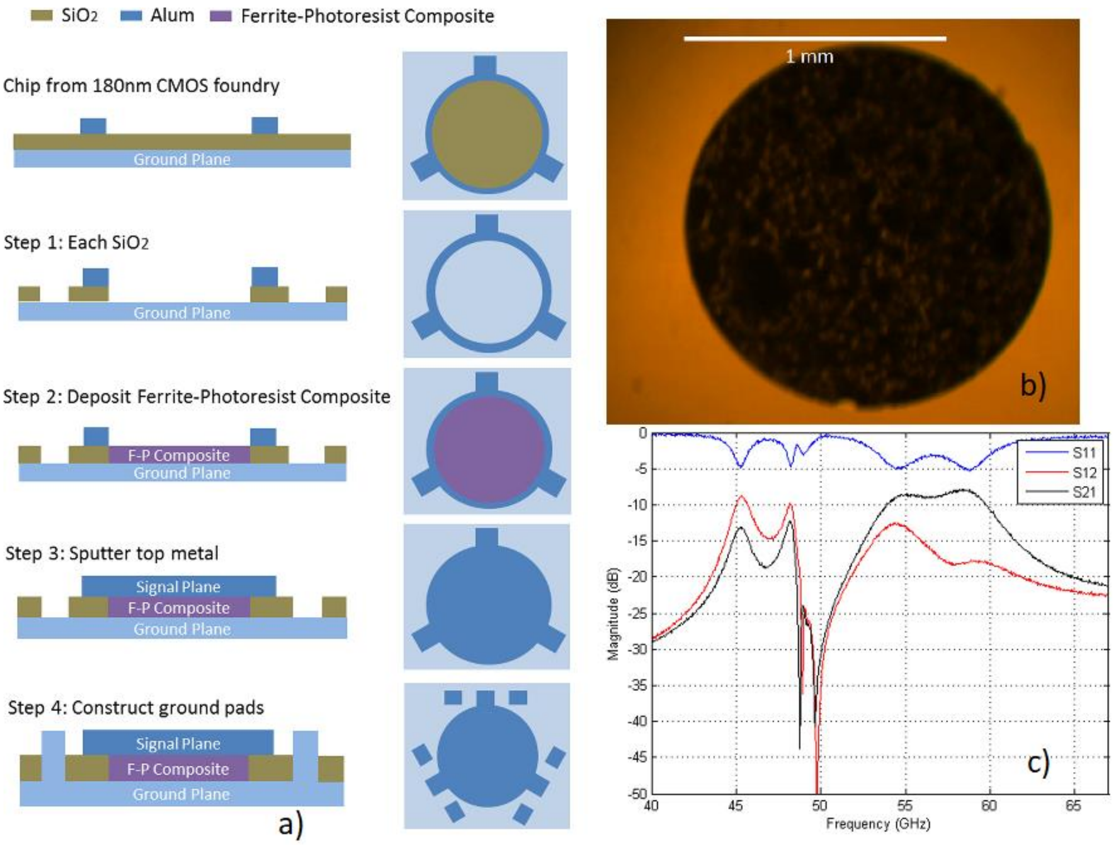

Figure 20 a) post-processing steps to the prototype chip: left side shows the cross-section view; right side shows the corresponding top view of the CMOS circulator, b) top view of circulator after ferrite/photoresist composite deposition, and c) Measured S-parameters of the fabricated prototype circulator by terminated the third port with a 50X load. The circulator shows the nonreciprocal properties from 55 GHz to 60 GHz [21]

Since the maturation and decreasing cost of FDM/FFF-type 3D printing, researchers have attempt to print with the magnetic-particle-with-polymer-matrix filaments. The filaments are usually manufactured in the fashion described above, but instead of casting into a final shape, the mixture is extruded to form spools of filaments which are later fed to a 3D printer. The final structure is formed by the extruded filament from the nozzle of a printer. This technique has achieved different levels of success [10], [11], [55], [56], as shown in Fig. 21; however, there exists a several common issues. First, due to the magnetic particles inside the polymer matrix, the flexibility of the filament becomes an issue. The filaments for 3D printers are usually folded to form spool for storage so if the magnetic particle concentration is too high, then the filament is not flexible to fold and could break. Second, as it is shown in Fig. 21 b) and c), the texture of the printed surface tends to be rough due to the magnetic particles. This could become a problem depending on the application of the printed structure and certainly for dimensional tolerance. Third, the magnetization tends to be isotropic for this time of composite. Without poling, there is little to no magnetic anisotropy.

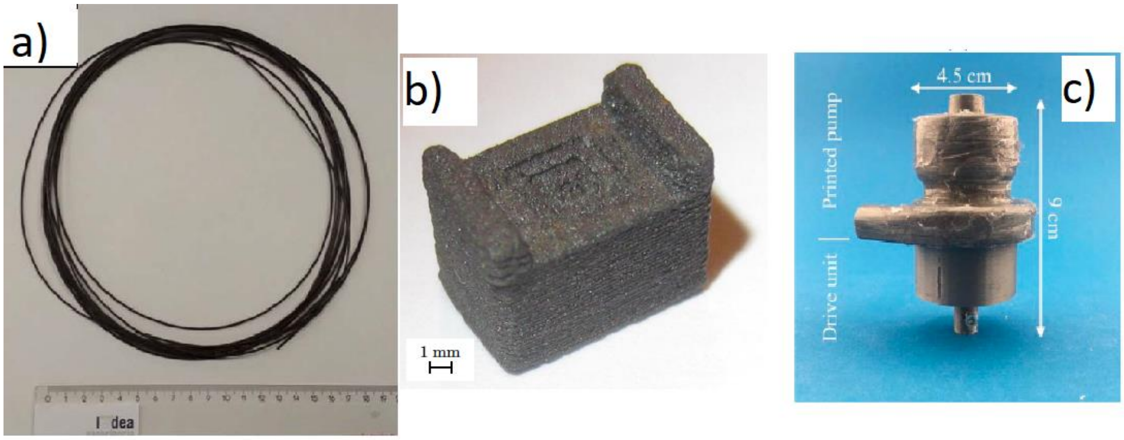

Figure 21 a) a filament of strontium hexaferrite and polymer composite [11] *b) a 3D printed isotropic NdFeB magnet* [10] *c) a fully printed motor pump* [56]

Using gel-like composite instead of solid or thermoplastic filament in 3D printing has also been studied [14], [15], [57]–[60]. The earliest effort, led by Lewis *et al.*, was developed before the term, “3D-Printing,” became well known. The first effort started with the study of adjusting the interaction force between particles in a dispersion, or slurry. As the technique matured, it was applied as an "ink" to directly write, or deposit to make complex structures. The interaction force between particles, as it changes, affects the mechanical properties, such as the modulus of the entire composite. Fig. 22 shows how the modulus can be tuned through the zeta potential of the particles. This technique allows the researchers to achieve different mechanical properties using the same base polymer matrix and print together as needed.

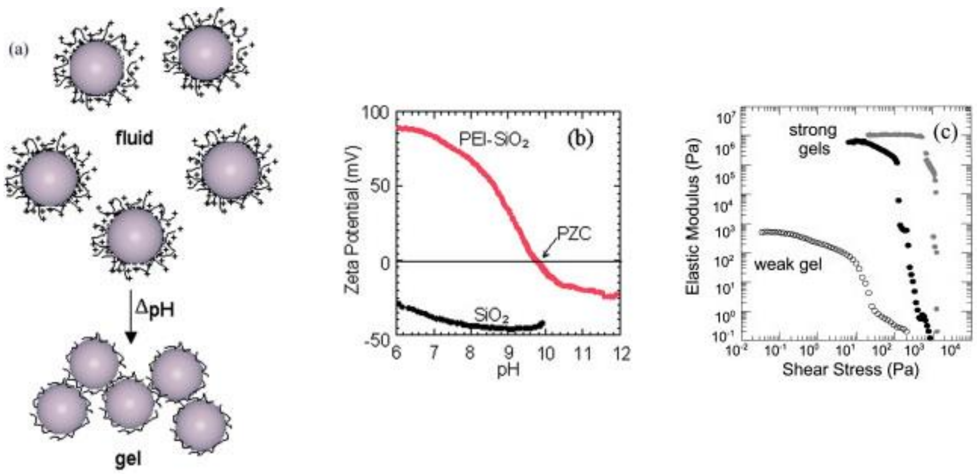

Figure 22 a) schematic illustration of fluid-to-gel transition observed for colloidal ink. b) A plot of zeta potential vs. pH for bare and PEI-coated silica microspheres suspended in water. c) The corresponding log-log plot of their shear elastic modulus vs. shear stress for concentrated silica gels of varying strength: open symbols denote weak gel (pH 9.5), black symbols denote strong gel (pH 9.75), and gray symbols denote strong gel (in oil) [61].

3D printing gel-like composite of polymer matrix with hard magnetic particles inside, on the other hand, is still a new fabrication technique in development [9], [13], [16], [55], [56], [62]. Based on the technique developed by Jennifer Lewis *et al.* [14], Yoonho Kim *et al.* incorporated hard magnetic material, NdFeB, into a silicone-based matrix [16]. With computer-aided design and customized print heads on a 3D printer, the group was able to print programmed ferromagnetic domains in soft materials that enable fast transformations between complex 3D shapes via magnetic actuation. The schematic in Fig. 23 summarizes how the simultaneous printing and poling works. The work allows great versatility in creating arbitrary 3D shapes and in-situ poling of the magnetic particles inside the polymer matrix; however, the configuration used only allows in-plane poling.

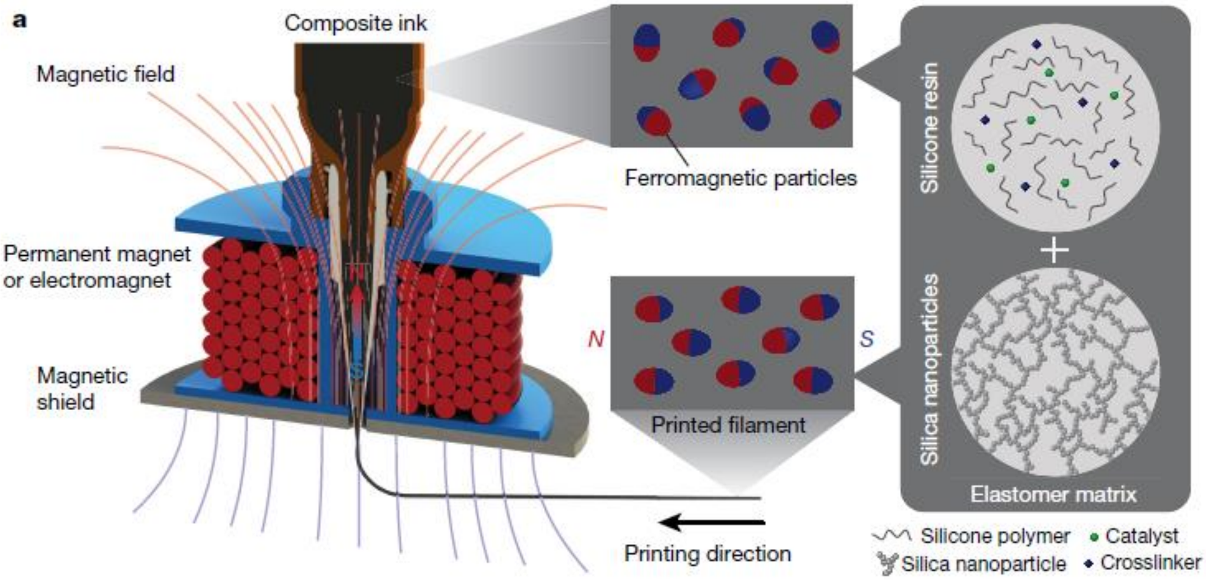

Figure 23 Schematic of in-situ, in-plane poling of magnetic composite [16]

The photosensitive polymer matrix used in this project, SU8, is liquid in room temperature. This makes the composite a combination of two phases, solid and liquid; such a mixture is called slurry. How a slurry behaves depend on a number of conditions such as particle size, viscosity of the liquid, flow velocity, flow direction, and other properties [63]. For the application of 3D printing, the composite will flow in the vertical direction. The two main criteria of a composite suitable for 3D printing are laid out in previous work [14]. The first criterion is a well-controlled viscoelastic response so it flows through the printer nozzle and then sets, or hardens, immediately to retain the shape of the deposited features. The second criterion is that the volume change should be small enough that the particle network is able to resist compressive stresses arising from capillary tension. For the purpose of this work, since the hexaferrite particles also need to rotate freely in the polymer matrix In order to be poled, an additional criterion is that the particles must be suspended in the matrix well as the composite is extruded through the nozzle. The criteria is expressed quantitatively by the particle Reynolds number. The number is calculated by the following equation: $R_e = \frac{\rho V l}{\mu}$, where ρ is the density of the liquid, *V* is the velocity of the liquid, *l* is the characteristic length of the particles, which is their diameter in this case, and μ is the dynamic viscosity of the liquid. In order for the mixture to behave as a homogenous entity, the particles need to be suspended in the liquid easily. If R_e is less than 0.1, then this condition is achieved. Using this value as the critical factor and other known range for the other variables in the equation, the necessary viscosity can be estimated. The equation above for Re can be further reduced if kinematic viscosity, ν, is used instead of dynamic viscosity. The relation between kinematic and dynamic viscosity is shown in the equation: $\nu = \frac{\mu}{\rho}$, the ρ here is also the same as the one in the Reynolds number equation, the density of the liquid. After some substitution, the equation for Reynolds number is now

$Re = Vl/\nu$. Now we just need to know the range of the velocity of the liquid and the diameter of particles to determine the kinematic viscosity needed to keep the composite homogenous.

Table I: Specifications of Strontium Hexaferrite particles		
Particle Diameter	5.5-15.9	μm
Density	4.98	g/cm^3
Saturation Magnetization	268920	A/m
	0.3379	Tesla
Remanent Magnetization	124500	A/m
	0.1565	Tesla
Coercivity	86978	A/m
	1093	Oe

Using the limit, $R_e \geq 0.1$, the equation now becomes $0.1 \geq Vl/\nu$, or $\nu \geq 10Vl$. The value ν has to be greater than $10Vl$ for the composite to be homogeneous. Assuming the liquid velocity is roughly the print speed, then $V = 10\ mm/s$. From the vendor specification listed in Table I, the range of the particle diameter is known, which is ~6 to 16 um, and thus the upper limit of particle diameter is $l = 1.6 * 10^{-5}\ m = 1.6 * 10^{-2}\ mm$. Using these values in the equation, $\nu \geq 10 * 10 * 1.6 * 10^{-2}$. The kinematic viscosity has to be greater than 1.6 mm^2/s or 1.6 cSt. With this limit, one constraint for the liquid polymer is set.

As the volume concentration of strontium hexaferrite increase in the liquid polymer, the composite becomes a shear-thinning fluid. The meaning of a shear-thinning fluid means that the viscosity decreases as the shear rate of the fluid increases. As it is proven experimentally later, the viscosity of the entire composite increases as the hexaferrite concentration increases, especially in lower shear rate. In fact, at 20% concentration, the viscosity is 4 orders of magnitude higher than that of pure SU8-2000.5 at rest. This behavior has been predicted for all slurries, but the volume concentration for the onset of this phenomenon seems much lower than the theoretical value [63]. While the cause of this phenomenon has not been thoroughly investigated for this study, it was studied in literature [14], [64], [65]. In the prior art, the suspended particles studied do not have strong particle-particle interactions. In the case of hexaferrite particles, this interaction force is much stronger due to the magnetization from strong MCA, magnetocrystalline anisotropy; this difference alludes to the low volume concentration of shear-thinning behavior. This non-Newtonian behavior will in turn makes the poling of the composite a more difficult and complex task. To avoid this behavior in the composite, the volume concentration of hexaferrite may need to be kept under 10%. However, since hexaferrite is the active material of the composite, if the concentration becomes too low, the magnetic properties may become negligible and thus no longer usable.

To achieve printing magnetization in all principal directions in space, poling in both in-plane and out-of-plane are needed. The in-plane poling means simply to pole the hexaferrite particles in the direction of the nozzle. Since the nozzle moves freely in the plane of printing, poling along the direction of the nozzle means magnetization will be in the direction of print head motion, which accounts two of the three principal directions. The out-of-plane poling means that the direction of the magnetization will be orthogonal to the print direction so it will always be pointing out of the plane of printing. Poling in these two directions can be achieved in two ways: in-situ and post-printing. In-situ poling means poling the composite while the printing takes place. Post-printing poling means poling the entire sample after the printing is finished. The concept of in-situ poling is illustrated in Fig. 24 and 25. Fig. 26 shows a prototype of an in-plane in-situ poling setup using an electromagnet.

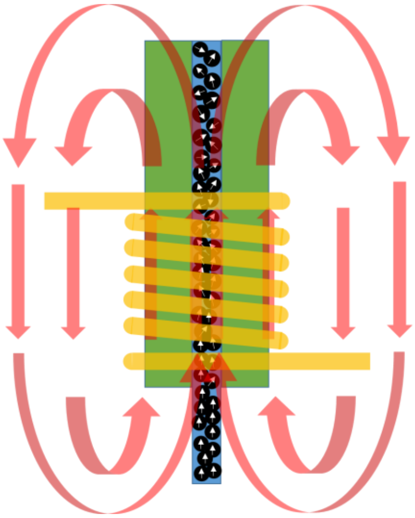

Figure 24 In-plane in-situ poling schematic, the red arrows show the direction of the field from the copper coil (in yellow)

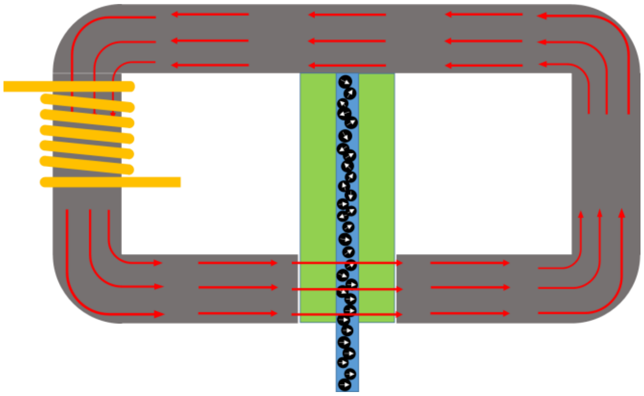

Figure 25 Out-of-plane in-situ poling schematic, the red arrows, which travel inside a soft, ferromagnetic material (in grey), show the direction of the field from the copper coil (in yellow)

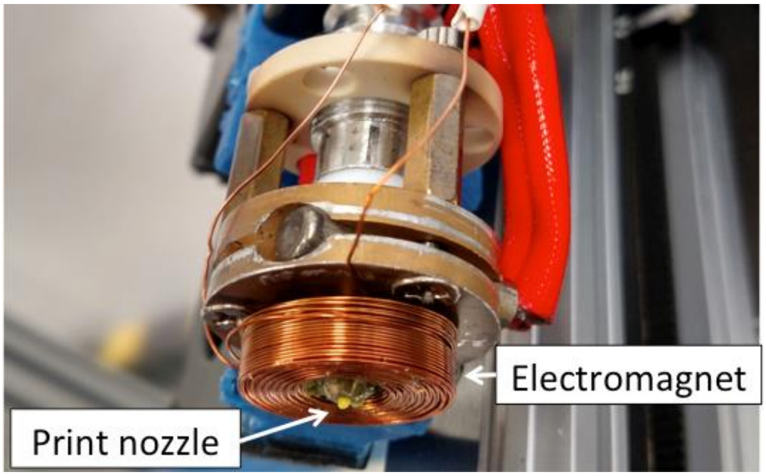

Figure 26 Prototype of in-plane in-situ poling

In theory, the in-situ method enables printing multiple zones of magnetization in different orientation within a printed structure, especially with an electromagnet. Electromagnets have a problem with resistive heating because it usually requires either a large electrical current or a high number of turns per unit length, unfortunately. Using permanent magnets for in-situ poling setup sacrifices some freedom but eliminates the need for a current supply and cooling. Fig. 27 shows an in-plane in-situ poling setup with permanent magnets.

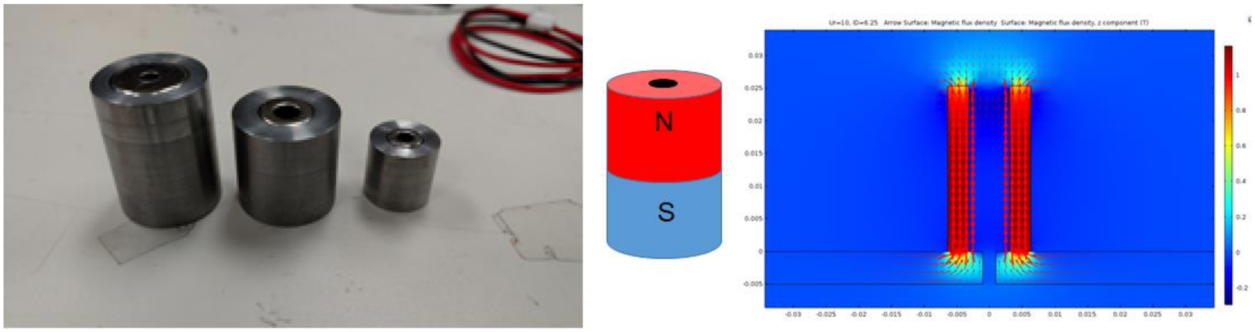

Figure 27 The photo on left is the actual magnets placed inside steel sleeves, and the middle illustration shows the magnetization of the magnets. The left schematic shows the simulation of the magnetic field direction inside the center hole of the magnets.

With post-printing method, the entire printed sample would have a uniform, one-direction magnetization and would therefore be less versatile. On the other hand, the post-printing poling would have a simpler setup. An illustration of the post-printing poling setup is shown in Fig. 28.

The schematic on the right shows the simulation of the permanent magnet on the left. The red arrows shows the field directions coming out of the magnet and would therefore turn the hexaferrite particles in the composite in out-of-plane direction.

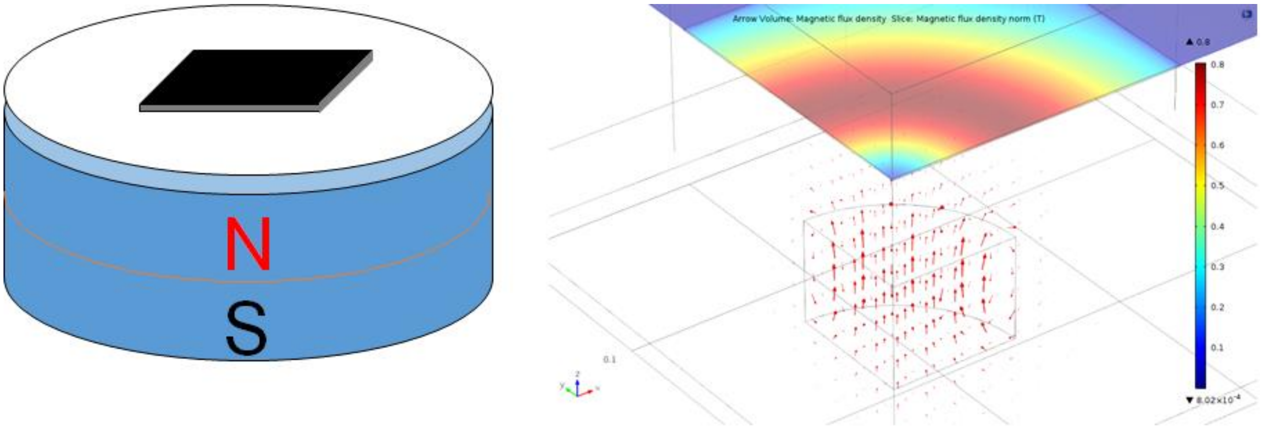

Figure 28 Out-of-plane post-printing poling setup. The schematic of the left is a permanent magnet, and the figure on the right is the simulation of such a magnet made of NdFeB. The red arrows in the right figure indicates the magnetic field direction, which should be the poling direction, out of the print plane.

The theoretical limits of poling magnetic particles were calculated by Stoner and Wohlfarth [66], and the concept is illustrated in Fig. 29. The angle shown in the legends are the angle θ shown in the inserted figure in Fig. 29 in degrees. The *M/Ms* of y-axis is the magnetization of the material normalized against the saturation magnetization; the H/Ha of x-axis is the applied magnetic field normalized against the anisotropy field, Ha. The anisotropy field of the hexaferrite particles comes mostly from MCA. The curves show the alignment of a single-domain particle; however, they can also be consider as the alignment of net magnetization of a group of single-domain particles. The most important feature of the figure is that if all the particles are perfectly aligned with the direction of the magnetic field, then the remanence would be zero when measured in the orthogonal direction.

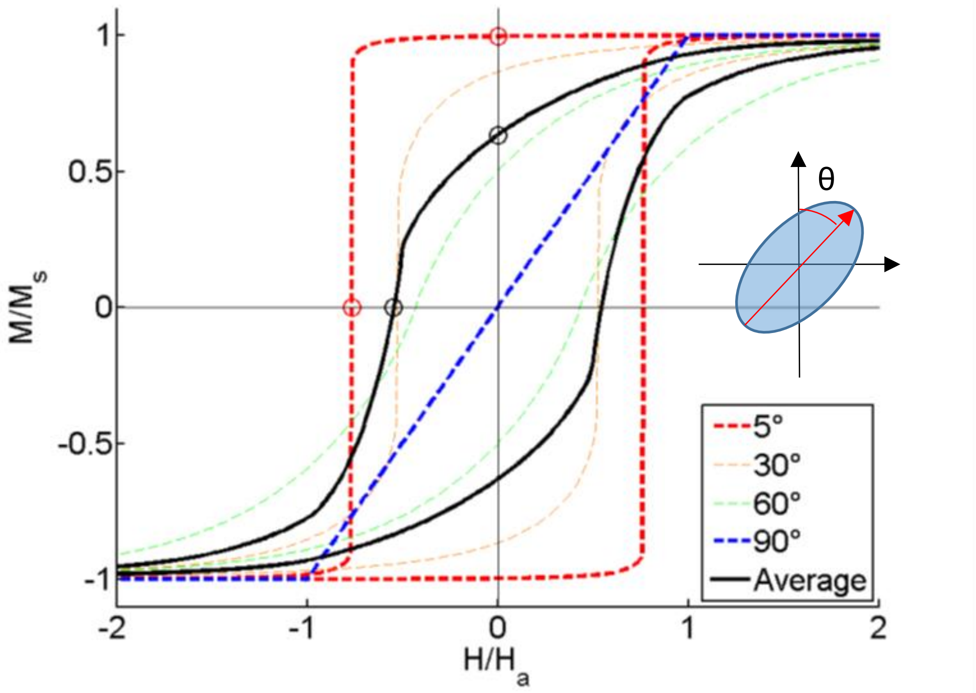

Figure 29 Magnetization curves for prolate spheroids. The M/Ms axis is the magnetization of the particle over the magnetization saturation of the material. The H/Ha axis is the applied field strength over the anisotropy field. The angle between the applied magnetic field and the easy axis of the material is given by θ.

Section 2.4: Ferromagnetic Resonance (FMR)

Ferromagnetic resonance, aka gyromagnetic resonance, originates from the precession of electrons in a ferromagnetic material in the presence of an external, time-varying magnetic field. The concept of precession is illustrated in Fig. 30, and it is well analyzed in the book written by Pozar [41]. The treatment in the book is reiterated here: when an external magnetic field, $\vec{H},$ is applied, an electron with a magnetic moment, $\vec{m}$, experiences a torque, $\vec{T}$. The torque can be calculated in the equation:

$$\vec{T} = \mu_o \vec{m} \times \vec{H} \quad \text{(2- 20)}$$

where $\mu_o$is the vacuum permeability. The torque causes precession of the electron around the direction of the applied field. Torque is equal to the change of angular momentum with regard to time, or like Eqn. 2-21 describes,

$$\frac{d\vec{s}}{dt} = \mu_o \vec{m} \times \vec{H} \quad \text{(2- 21),}$$

where $\vec{s}$ is the angular moment. The relationship between angular moment and magnetic moment due to the electron spin can be described by the equation

$$\vec{m} = -\gamma \vec{s} \quad \text{(2- 22),}$$

where $\gamma = 1.759 \times 10^{11}\ C/kg$ is the gyromagnetic ratio. If Eqn. 2-21 and 2-22 are combined, then the time derivative of magnetic moment can be calculated as:

$$\frac{d\vec{m}}{dt} = -\mu_o \gamma \vec{m} \times \vec{H} \quad \text{(2- 23).}$$

Through the mathematical treatment by Pozar [41], the precession frequency of the electrons in the presence of a magnetic field is $\omega_o = \mu_o \gamma H$, where H is the field strength of the magnetic field. For hexaferrite materials, however, there could be demagnetization factor due to their shape. Naturally occurring hexaferrite particles typically possess flake-like or shapes with high aspect ratio. This type of shape causes high demagnetization factor and thus decrease the effective bias field. After the demagnetization factors are taken into account and some algebraic manipulation, the precession frequency can be calculated in the following equation:

$$\omega_0 = \mu_0\gamma\sqrt{[H_a + (N_x - N_z)M_s][H_a + \left(N_y - N_z\right)M_s]} \qquad \text{(2- 24),}$$

where N_x, N_y and N_z are the demagnetization factors of the x, y, and z axes, respectively and M_s, is the saturation magnetization of the hexaferrite. This equation (2-24) is known as Kittel's equation. The MCA can be consider a source of the magnetic field. If the value of MCA in strontium hexaferrite is used in the equation, which is close to 2T, then the FMR frequency is 56 GHz if the shape of the particles are mostly spherical. If the shapes of the particles are mostly flake or disc like, then $N_x = N_y; N_z \cong 1$, and the FMR frequency becomes ~51GHz. These frequencies are close to the frequency of interest.

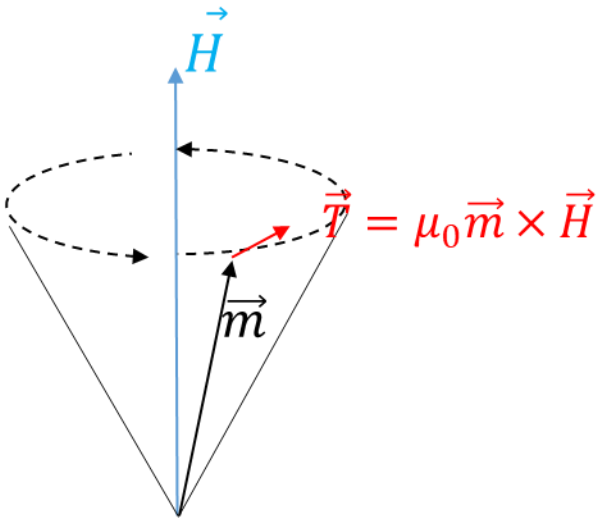

Figure 30 FMR Schematic, where $\vec{H}$ is the external magnetic field, $\vec{m}$ is the magnetic moment of an electron, and $\vec{T}$ is the torque acting on the electron from the two interacting. As a result, the electron process around the direction of $\vec{H}$ as shown

Section 2.5: Process WIndow

Through the constraints and the needs of the application (ferrite circulator), a set of requirements can be determined for the composite of polymer and hexaferrite particles:

1. The composite must maintain its shape after deposition.
2. The curing of the composite must not change its volume too much.
3. The viscosity of the composite must be high enough for a filament-like deposition on a FDM 3D printer.
4. The viscosity of the polymer matrix must be low enough so that the hexaferrite particles can rotate fast enough.
5. R_e must be low enough for good particle distribution.
6. The hexaferrite particles in the composite must be as spherical as possible.
7. The concentration of the hexaferrite particles in the composite must be high enough that there is a FMR response.

If the composite can meet these requirements, then it can be 3D printed and used for circulator/isolator type of applications.

Chapter 3: Experimental Procedures

Section 3.1: Composite Fabrication

The composite is made of hexaferrite particles and a liquid polymer matrix. The strontium hexaferrite particles are provided by PowderTech Co., Ltd., and the properties of the particles are listed in Table I. The range of the particle diameter implies that the particles are probably multi-domain instead of single-domain [67]. This implication would explain the deviation of magnetic properties form those of bulk strontium hexaferrite found in literature. After the volume fraction of strontium hexaferrite is selected, the particles are weighed to have the correct volume. The SU8 2000 series photoresist by Microchem is chosen as the polymer matrix for the composite due to its low toxicity and selection in viscosity. The viscosities and densities of some of the models of the series are listed in Table II. One example is SU8 2000.5; its low viscosity (0.027 Poise), makes particle rotation inside the matrix easier. The volume of SU8 is measured by a syringe or graduated cylinder. The two types of SU-8 used in the study are SU8-2000.5 and 2005.

After the desired amount of each component is obtained, they are mixed together inside a planetary mixer, Thinky AR-100, for 1 minute. The mixer uses centripetal force to separate the magnetic particles inside the liquid polymer matrix and creates a uniform dispersion. This technique has been used in the past to create composite for 3D printing [68][16]. The particular Thinky mixer that was used is shown in Fig. 31.

Figure 31 Thinky AR-100, a centripetal mixer

While the particles are separated, due to the relatively low viscosity of the SU-8 used, they tend to settle to the bottle of the container quickly when there is no turbulence in the liquid matrix. As a result, agitating the composite before printing is necessary to ensure uniform distribution of the hexaferrite particles.

Table II: SU-8 2000 Viscosity

SU-8 2000 Series Model #	Viscosity (cSt)	Density (g/ml)
2000.5	2.5	1.07
2002	7.5	1.12
2005	45	1.16
2007	140	1.18

Section 3.2: Printing

The mixture is then poured into a syringe, which is part of the modular print head of a Hyrel 3D Printer, System 30M. The syringe extrudes the composite in the pattern programmed to the printed. The print head, along with the type of syringe used, is shown in Fig. 32. The syringe is equipped with a plastic needle that has an inner diameter of approximately 0.5 mm. The composite is typically printed on top of a substrate that lies on the print bed. A schematic of the printing setup is shown in Fig. 33.

Figure 32 Print head for hexaferrite-SU8 composite; the syringe can be purchased separately

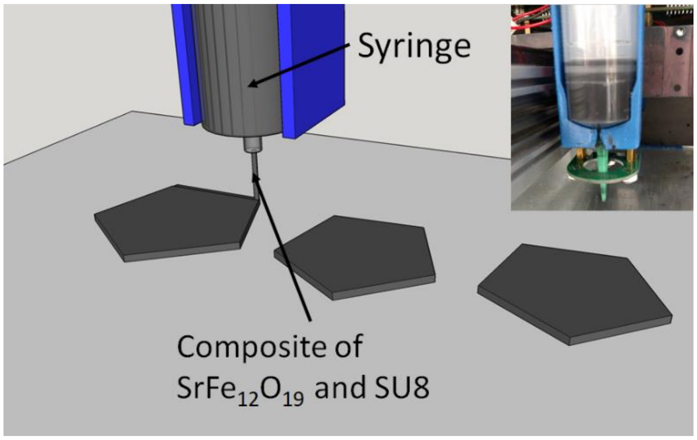

Figure 33 Schematic and photo of printing the composite; the inset is the actual setup with the UV light LED around the nozzle

Earlier research [14], [15] suggests that colloidal fluid suits FDM 3D printing because the fluid would retain its shape after it is printed. The mixture of strontium hexaferrite particles and SU8 photoresist does exhibit shear thinning behavior at different concentrations as characterized in Chapter 4.1. The viscosity and degree of shear thinning both increase as the volume concentration of the strontium hexaferrite is increased. The cause of this increase is most likely due to the increase in interaction between particles as the average distance among them decreases, as suggested by previous work [14].

Section 3.3: Poling and Curing

After the desired pattern of composite is printed, the sample and its underlying substrate are then placed on a poling device. The poling device provides a constant external magnetic field. The device for the sample presented here is a permanent magnet that provides a field of 270,000 A/m, or 0.34 T of magnetic flux, measured at the magnet surface. When the strontium hexaferrite particles in the composite experience the external magnetic field, they should rotate toward the field direction due to the torque produced between their magnetization and external field. The poling setup is shown in Fig. 24, 25, 26, 27 and 28. This technique has been previously demonstrated both in-situ and ex-situ [16], [68], [69]. The sample is left on the surface of the poling magnet to provide an initial curing of polymer. After 2 hours, the sample is then soft baked at 95°C to further remove the solvent from the composite. After soft baking for at least 10 minutes, the sample is then placed under UV radiation. The dosage of UV should be at least 160 mJ in accordance with the datasheet. After UV exposure to the photoresist-hexaferrite composite, the sample should be hard-baked at 95°C for another 10 minutes at least. Actual printed and poled samples are shown in Fig. 34 and 35.

Section 3.4: Results

The printed, poled, and cured samples are shown in Fig. 34 and 35. The substrate used in Fig. 34 is silicon and sapphire in Fig. 35, and both of the are 4-inch wafers. The technique is applicable to different type of substrates.

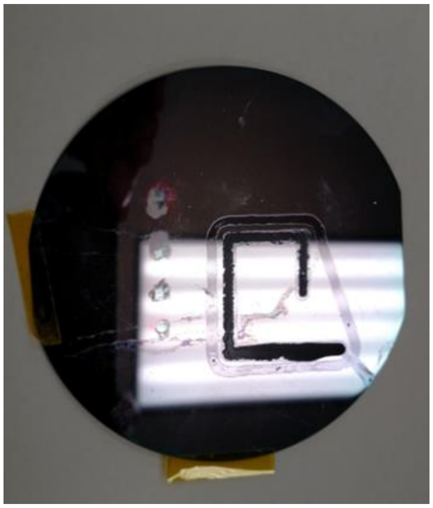

Figure 34 Printed sample on a 4-inch Si wafer

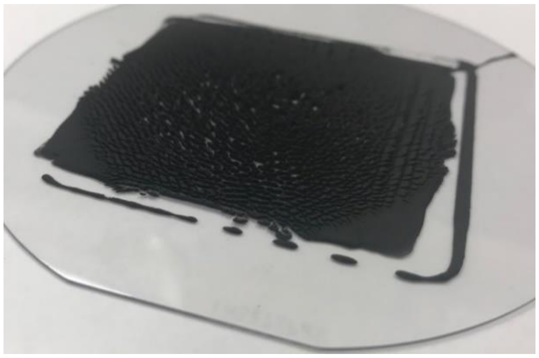

Figure 35 Printed sample poled out of plane on a 4-inch sapphire substrate

Chapter 4: Characterization and Analysis

Section 4.1: Viscosity Measurement

The importance of viscosity of the composite used has been established in Chapter 2.3 and work by Lewis *et al.* [14]. It must be high enough so that it would retain its shape after deposition, but low enough to allow rotation of hexaferrite particles under a magnetic field. The viscosity of the composite is measured by a desktop rheometer, TA Instruments AR2000, similar to the one shown in the insert of Fig. 36. This type of rheometer is a plate-plate-flow type. The composite is placed on a horizontal, flat surface, and a flat disc is placed against it, as shown in Fig. 36. The disc is then rotated by a motor and the torque on the disc is measured.

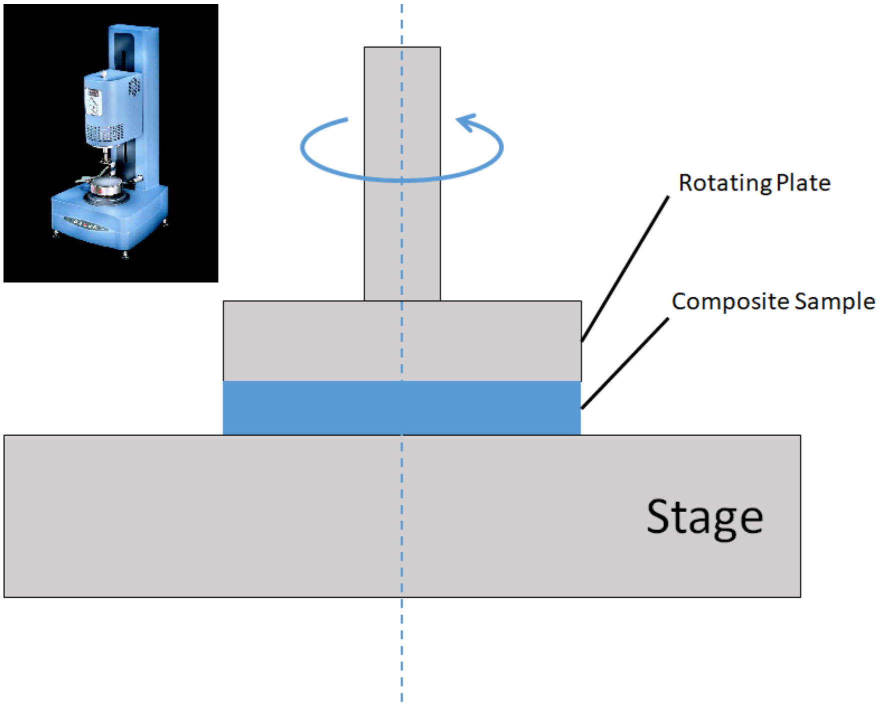

Figure 36 Schematic of a rheometer; inset: TA Instruments AR2000 Source: http://www.tainstruments.com/pdf/literature/ar2000

It is shown here that the mixture of strontium hexaferrite particles and SU8-2000.5 exhibits shear thinning behavior, as shown in Fig. 37.

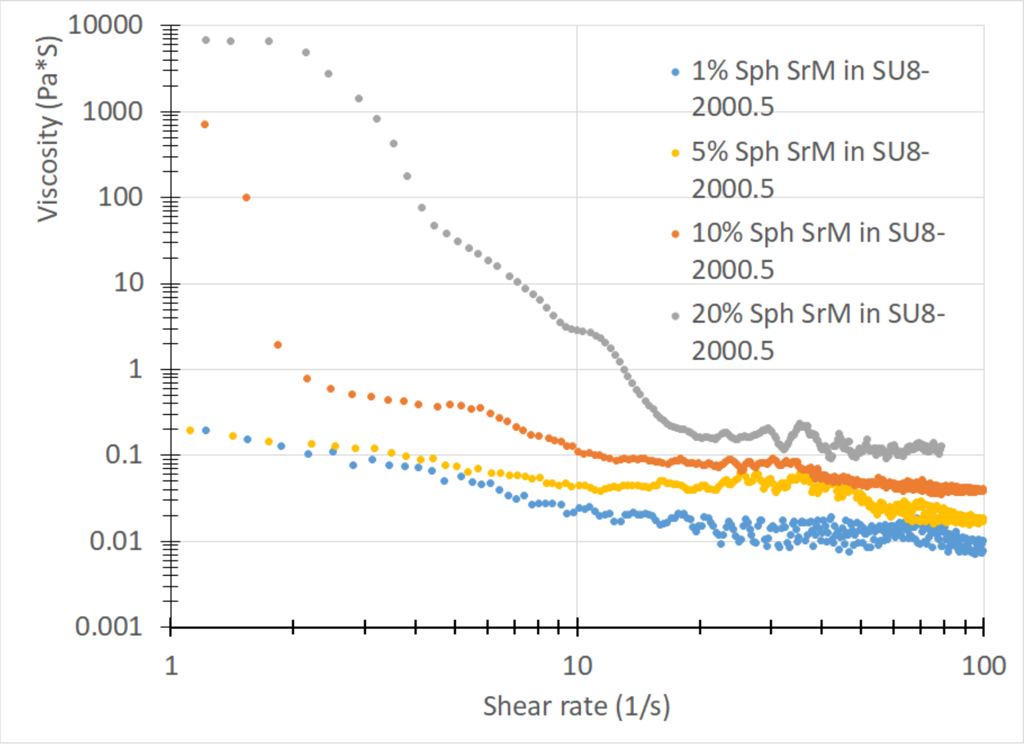

Figure 37 The viscosity of strontium hexaferrite-SU8-2000.5 mixture as a function of shear stress is tested at different concentration of the hexaferrite particles. The composites start to show large increase in shear thinning behavior when the volume concentration of SrM is over 10%

The viscosity and degree of shear thinning both increase as the volume concentration of the strontium hexaferrite is increased. The shear-thinning nature of the composite also implies that post-printing poling would require the most torque because viscosity would be the highest when the composite is at rest. What was observed during poling of different polymer matrix is there seems to be a viscosity in which the particles are allowed to rotate at rest; however, if the particle concentration is too high, they rotate as clusters as they rotate. The result is shown in Fig. 38; the surface of the composite spikes up due to the rotation of these clusters. As the resting viscosity of the polymer matrix gets higher, the rotation is suppressed. One of such spikes is taken and imaged in a scanning electron microscope (SEM); a representative image is shown in Fig. 39.

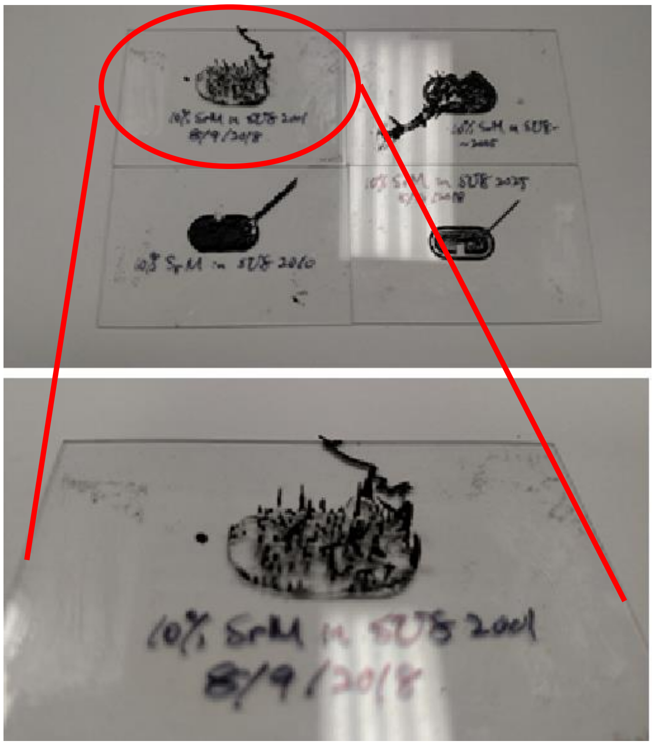

Figure 38 Spiking can occur if the concentration of hexaferrite particles get high enough, and as the viscosity of the polymer matrix increases, the spiking behavior diminishes

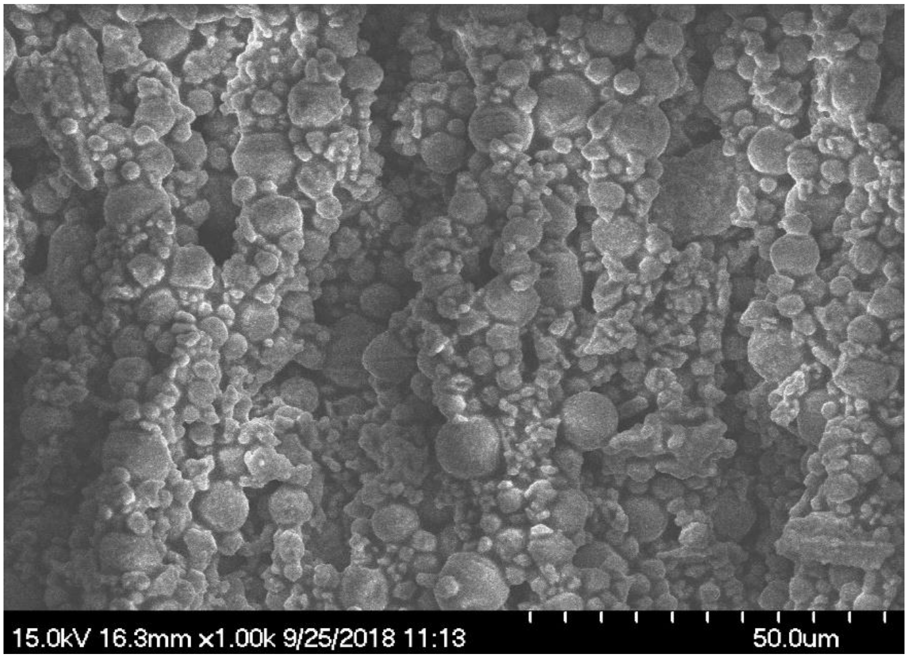

Figure 39 Cross section of pikey surface in SEM; the hexaferrite particles are seen clustering together

Through this chain of thinking, the rheological conditions for the composite can be established. If rotation of particles is needed without forming spikes, then not only does the viscosity of the polymer matrix need to be low enough, but the particles need to be far enough from one another so they do not form clusters. Since 10% volume concentration causes spiking and 1% is not enough to have a measurable FMR response, a good compromise seems to be 5% volume concentration. A different polymer matrix, SU-8 2005, was also tried; its rheological properties can be found in Table II. The variety of the SU-8 photoresists and their viscosity is shown in Fig. 40. The viscosity is adjusted by the amount of solid in the polymer. The 2005 model has viscosity that is one order of magnitude higher than that of SU-8 2000.5.

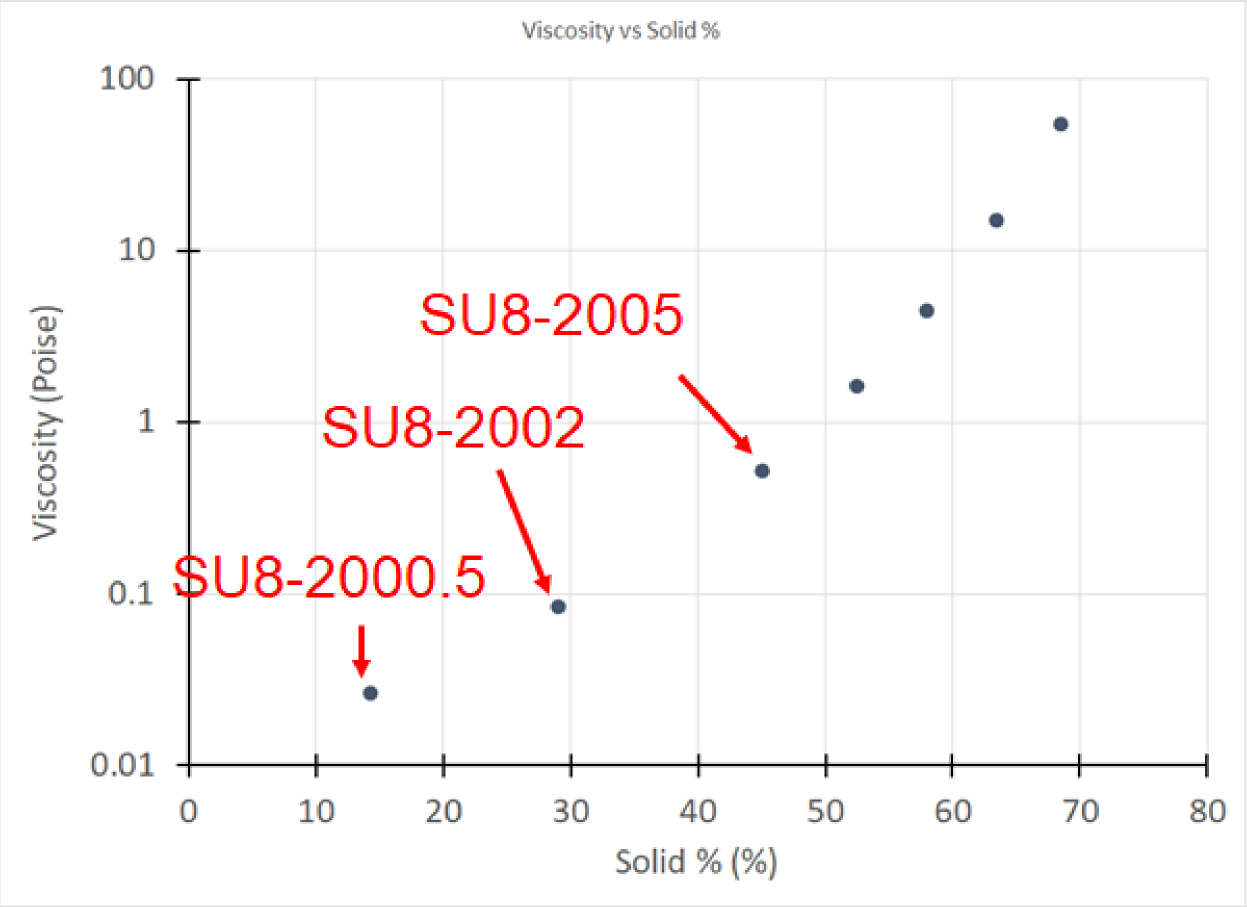

Figure 40 The viscosity of SU-8 2000 series. The solid % is also what distinguishes different models of SU8-2000 photoresists

The 5% composites of the two polymer matrixes are measured in the rheometer and compared in Fig. 41. The viscosity difference between the two composite is roughly about 1 order of magnitude, which originates from the difference in viscosity of the two polymer matrices.

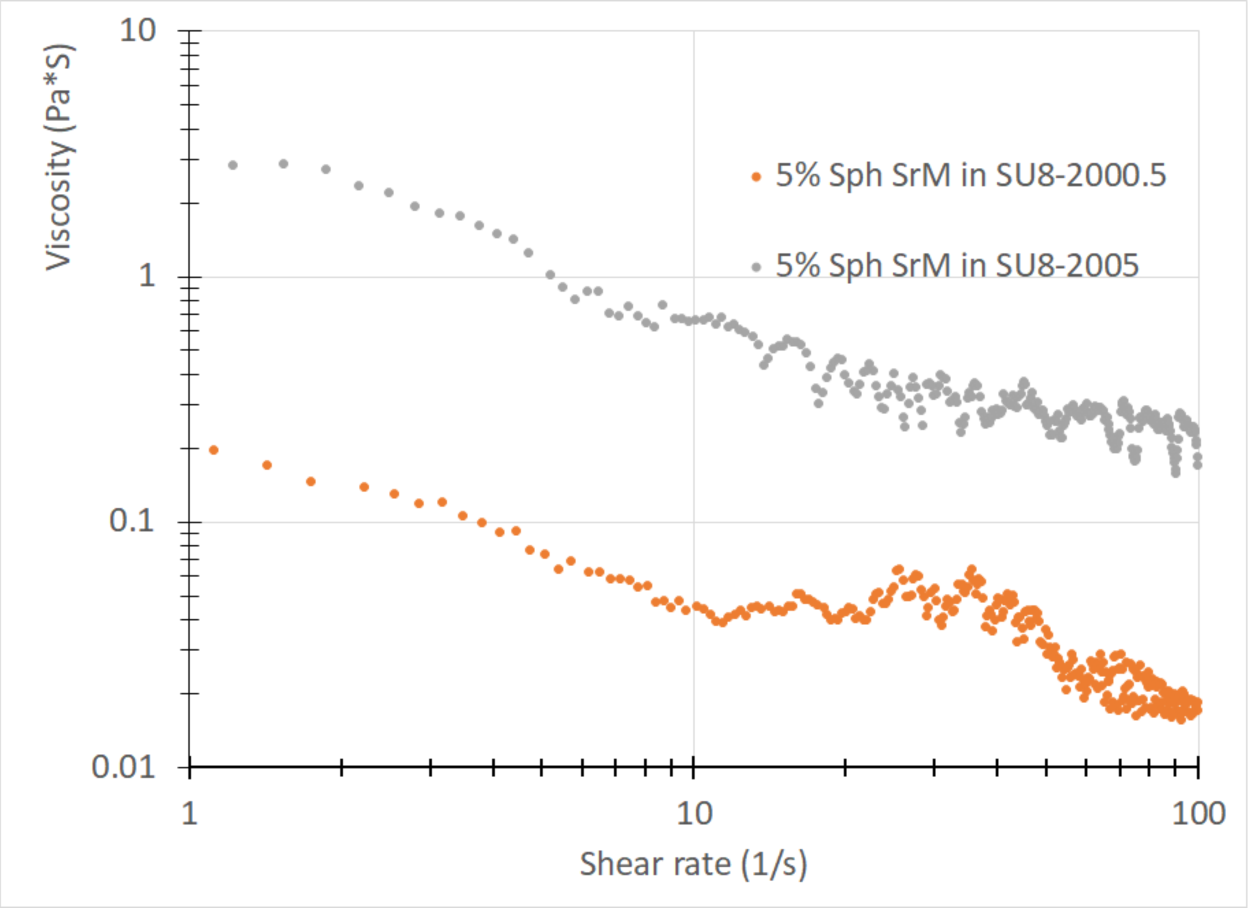

Figure 41 The viscosity comparison between the 5% composites of SU8-2000.5 and SU8-2005

With SU-8 2005 as the matrix, the 5% composite was made, printed, and poled on a 4-inch glass substrate as a test. An image of the sample is shown in Fig. 42. Comparing to the 10% samples of low viscosity, the surface of the cured 5% composite seems much smoother.

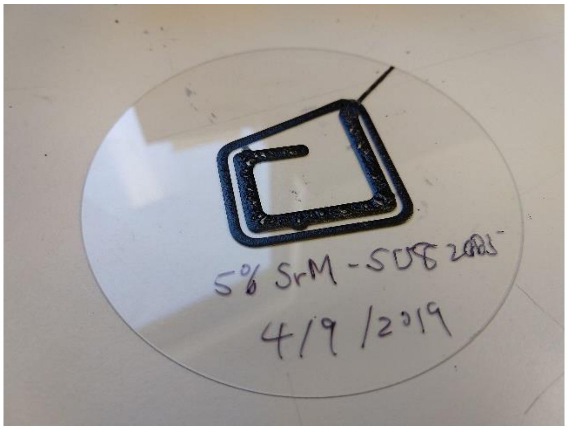

Figure 42 Printed, poled, and cured 5% SrM-SU-8 2005 composite, and there is no spikey surface

Section 4.2: SQUID/VSM Measurement

After the spiking issue is resolved by lowering the volume concentration of strontium hexaferrite particles in the composite, the magnetic anisotropy needs to be confirmed. The poled and cured sample is then measured inside a SQUID. SQUID stands for Superconducting QUantum Interference Device; it is a magnetometer that is capable of measuring magnetic fields of very low strength. The schematic of a SQUID is show in Fig. 43. Fig. 44 shows the particular SQUID used for measuring the samples, which is made by Quantum Design, and it consists of four superconducting loops containing Josephson junctions.

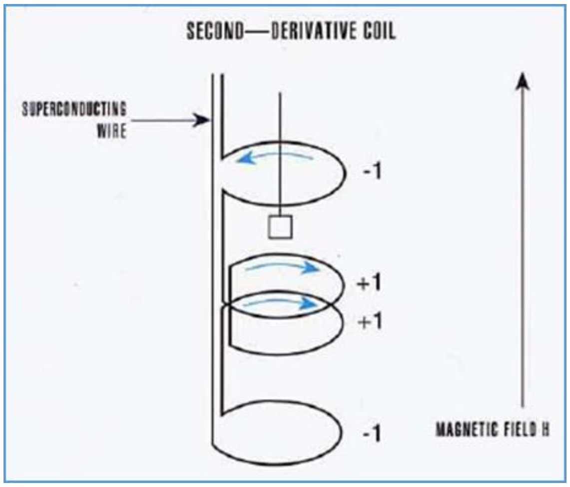

Figure 43 SQUID schematic [70]

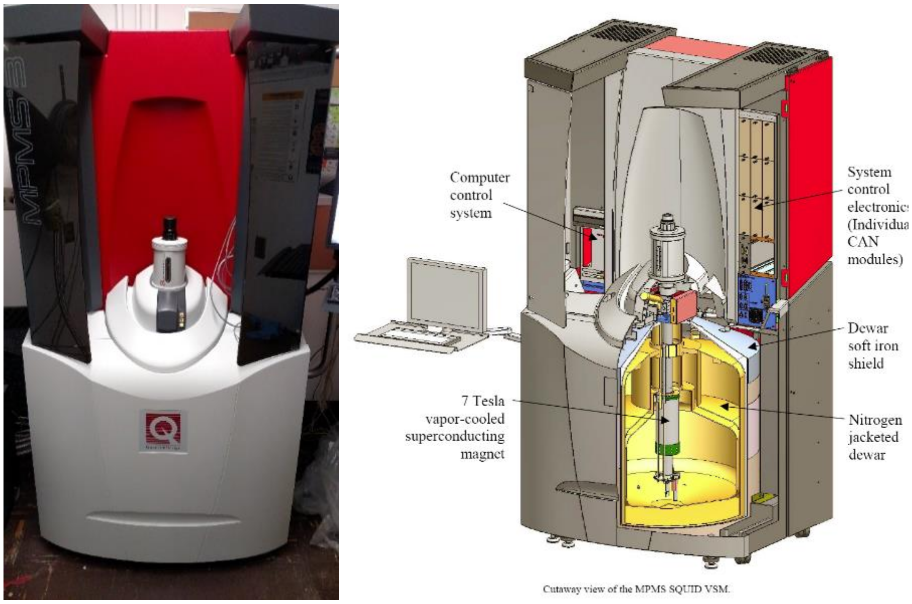

Cutaway view of the MPMS SQUID VSM.

Figure 44 MPMS3 SQUID/VSM by Quantum Design [70]

A SQUID, in particular the model MPMS3 made by Quantum Design, can measure a magnetic field in many modes. The mode used in this study is vibrating-sample magnetometer, or VSM. A schematic of VSM is shown in Fig. 45. A sample is put (usually vertically) in an external, uniform magnetic field. It is then sinusoidally vibrated perpendicularly to the field direction. The vibrating component causes a change in the magnetic field of the sample, which generates an electrical field in a coil based on Faraday's Law of Induction. The induced voltage in the pickup coil is proportional to the sample's magnetic moment, but does not depend on the strength of the applied magnetic field. The entire setup of the SQUID/VSM measurement is illustrated in Fig. 46. The signal picked up from the measured sample in VSM is calculated to extract the magnetic moment of the sample. The magnetic field applied can be up to 7 Tesla in this particular system.

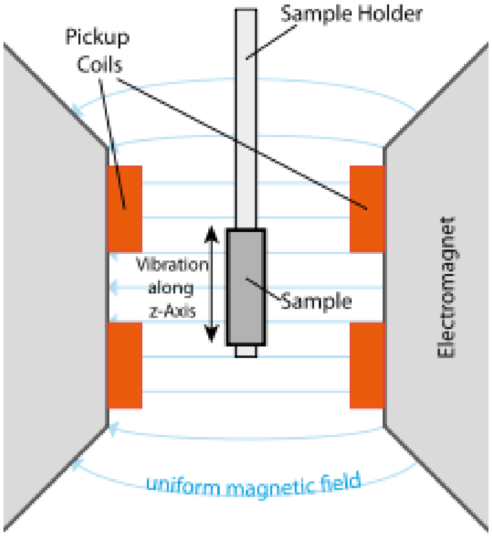

Figure 45 VSM schematic, the blue arrows shows the external magnetic field direction Source: wikipedia

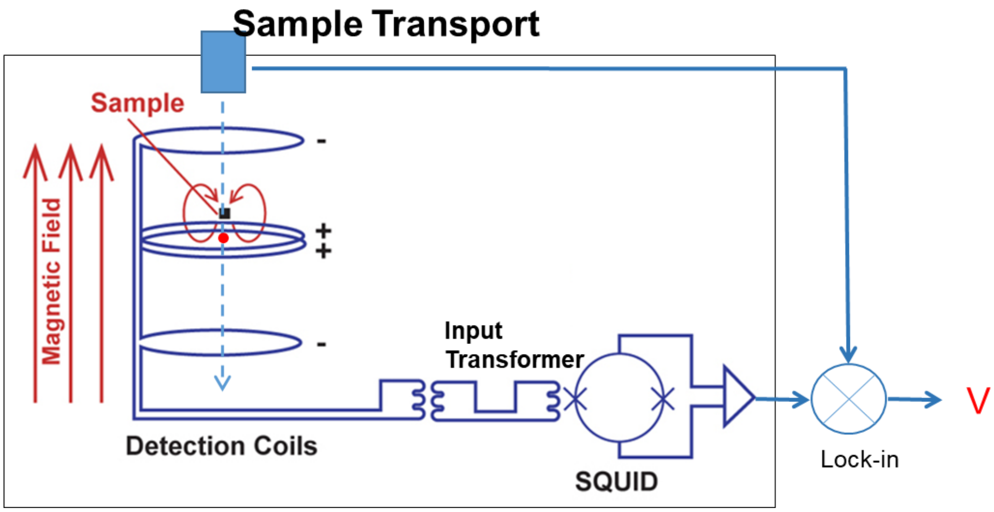

Figure 46 VSM using SQUID. Source: Quantum Design, Inc

To establish a reference of particle alignment, an "air bridge" sample was used. An air bridge is created by suspending hexaferrite particles in air between two opposite magnetic poles; the schematic of this sample is shown in the inert in Fig. 47. After the particles were suspended in the air by the magnetic field, they were glued together by epoxy. This cured piece serves as a reference on the uniformity of orientation of the strontium hexaferrite particles and thus magnetic anisotropy that could be achieved. As shown in the MH curve in Fig. 47, the difference in remanence in the two direction is about 20% of saturated magnetization (M_s), or squareness ratio. Squareness ratio, sometimes abbreviated as SQR, is remanent magnetization divided by the saturation magnetization of the material. Though it is far from the ideal case show in Fig. 29, this is the baseline of spherical strontium hexaferrite-SU8 composite rotation. Comparing this result to the thick film deposited using other technique like screen printing and sintering [32], which shows an anisotropy of 6x squareness ratio, this technique shows less anisotropy. Using this difference as the standard for anisotropy, how much have the composite samples can be compared.

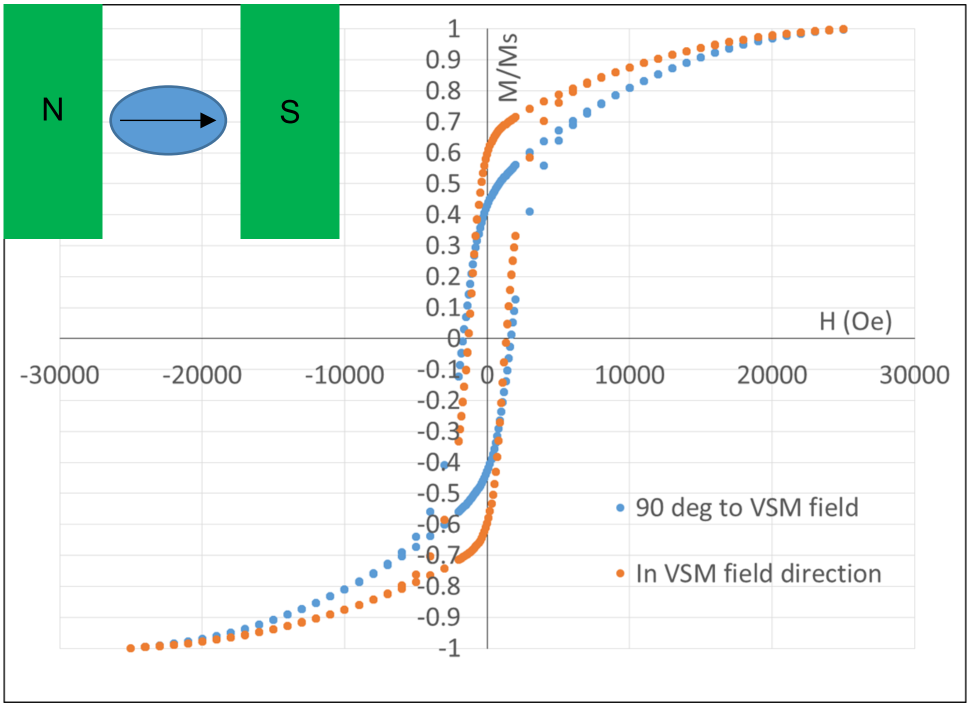

Figure 47 MH curve of an air bridge of strontium hexaferrite particles

To pole the composite out-of-plane, post-printing setup was used, shown in Fig. 28. The simulation of this setup is shown in Fig. 48. As it is shown in the figure, the B-field just above the setup can get as high as 0.8 Tesla, which would generate more than enough torque on the strontium hexaferrite particles to torque them under 0.1 second, which is about the time needed from the calculation shown in Fig. 17 in Chapter 2.2. The samples were left on the poling setup for over 1 hour to ensure complete rotation. The results have been shown in Fig. 34 and Fig. 35.

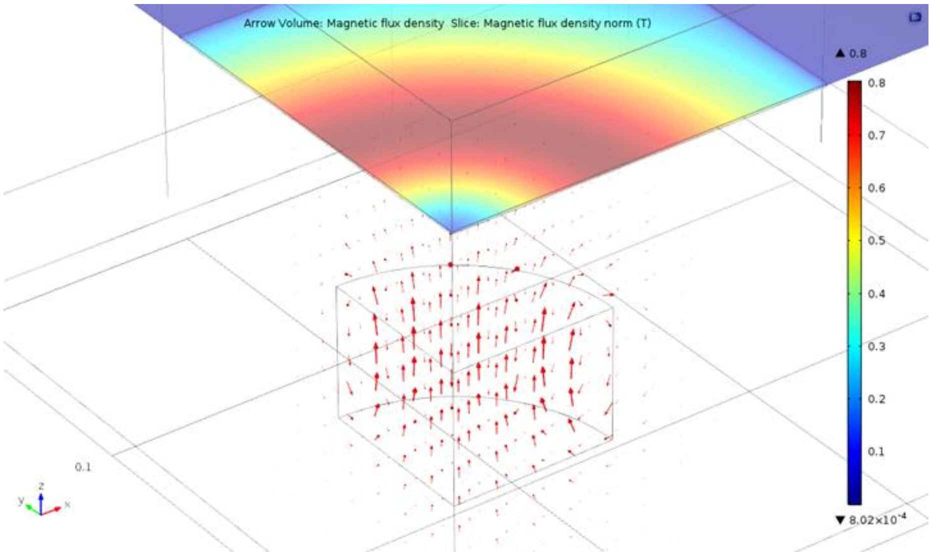

Figure 48 COMSOL simulation of post-printing out-of-plane poling setup; the red arrows show the direction of the magnetic field from the magnet itself.

Although the surface is not quite flat on the 10% composites of SU8-2001 and 2005, the magnetic anisotropy can still be tested. One of such spikes was taken and measured in the SQUID/VSM, and the result is shown in Fig. 49. The anisotropy measured is about 16% difference in squareness ratio, and it is on par with the air bridge reference. However, spikey surface would make monolithic integration with MMIC or other 2D-like technology. Therefore, the 5% strontium hexaferrite-SU8 2005 composite is used and should achieve the best compromise of anisotropy and surface smoothness. The sample from Fig. 42 was measured in the SQUID/VSM, and the result is shown in Fig. 50.

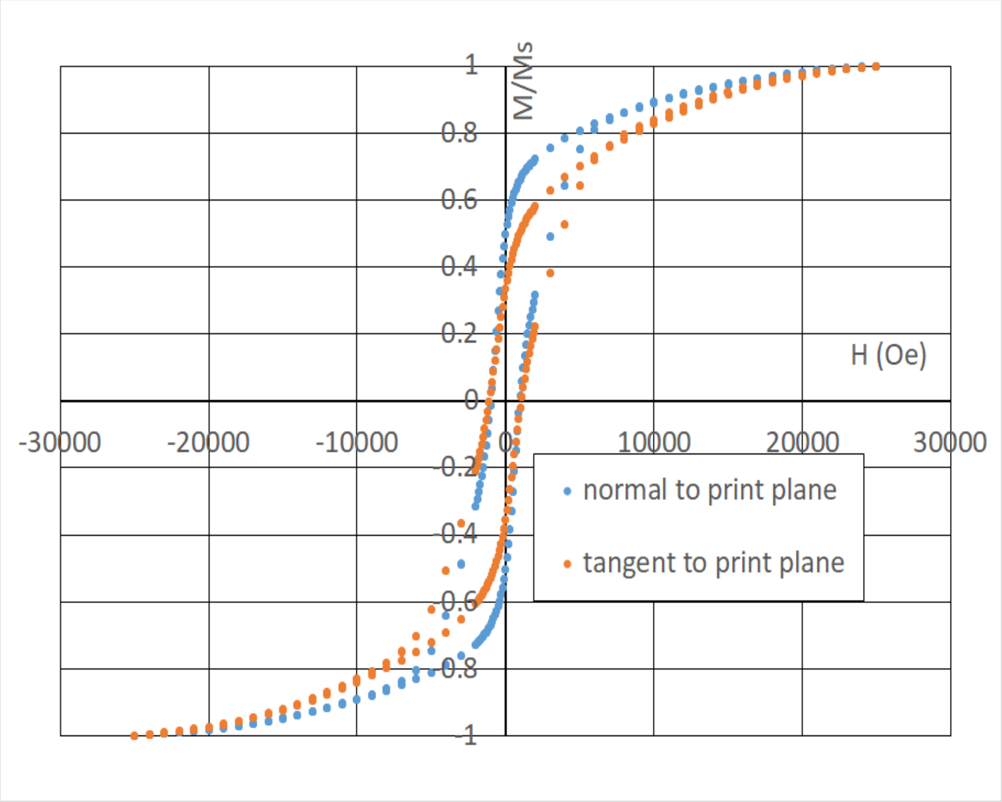

Figure 49 MH curves of posting-printing, out-of-plane poling of a 10% SrM-SU8 2000.5 composite, the difference in remanence in the two axes is about 16%

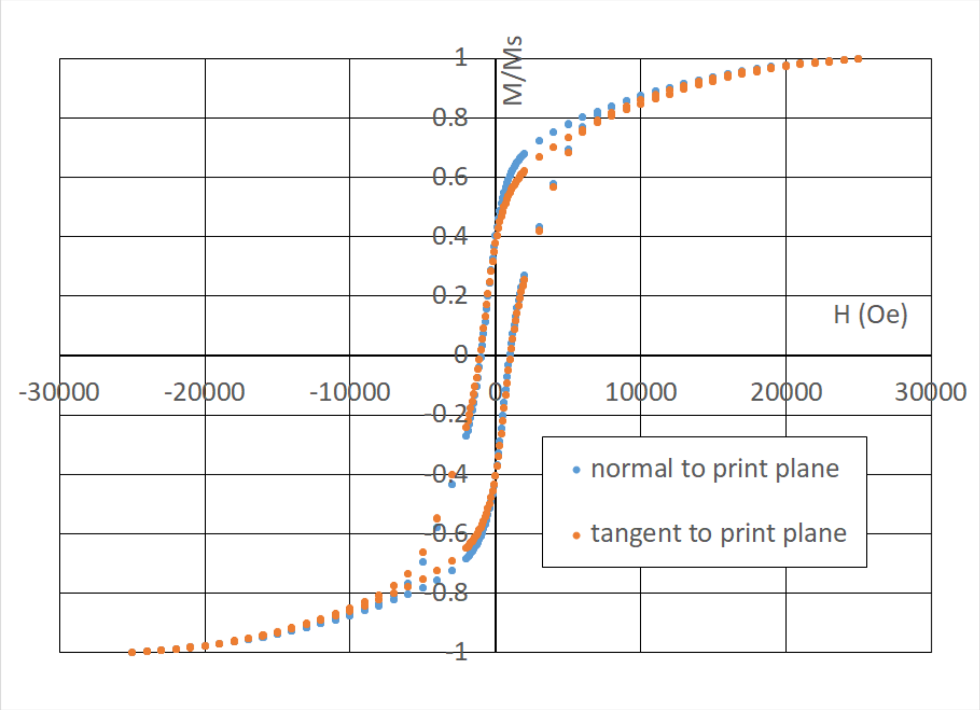

Figure 50 MH curves of posting-printing, out-of-plane poling of a 5% SrM-SU8 2005 composite, the difference in remanence in the two axes is about 3%

There is significant anisotropy but at a much smaller difference in squareness ratio, about 3%.

Though not applicable to the circulator application, the in-plane in-situ poling setup shown in Fig. 27 was implemented and tested. The same ideal composition, 5% SrM in SU8-2005 was printed and pole in-situ. The printed sample was cured and tested in SQUID/VSM, and the MH curves are shown in Fig. 51.

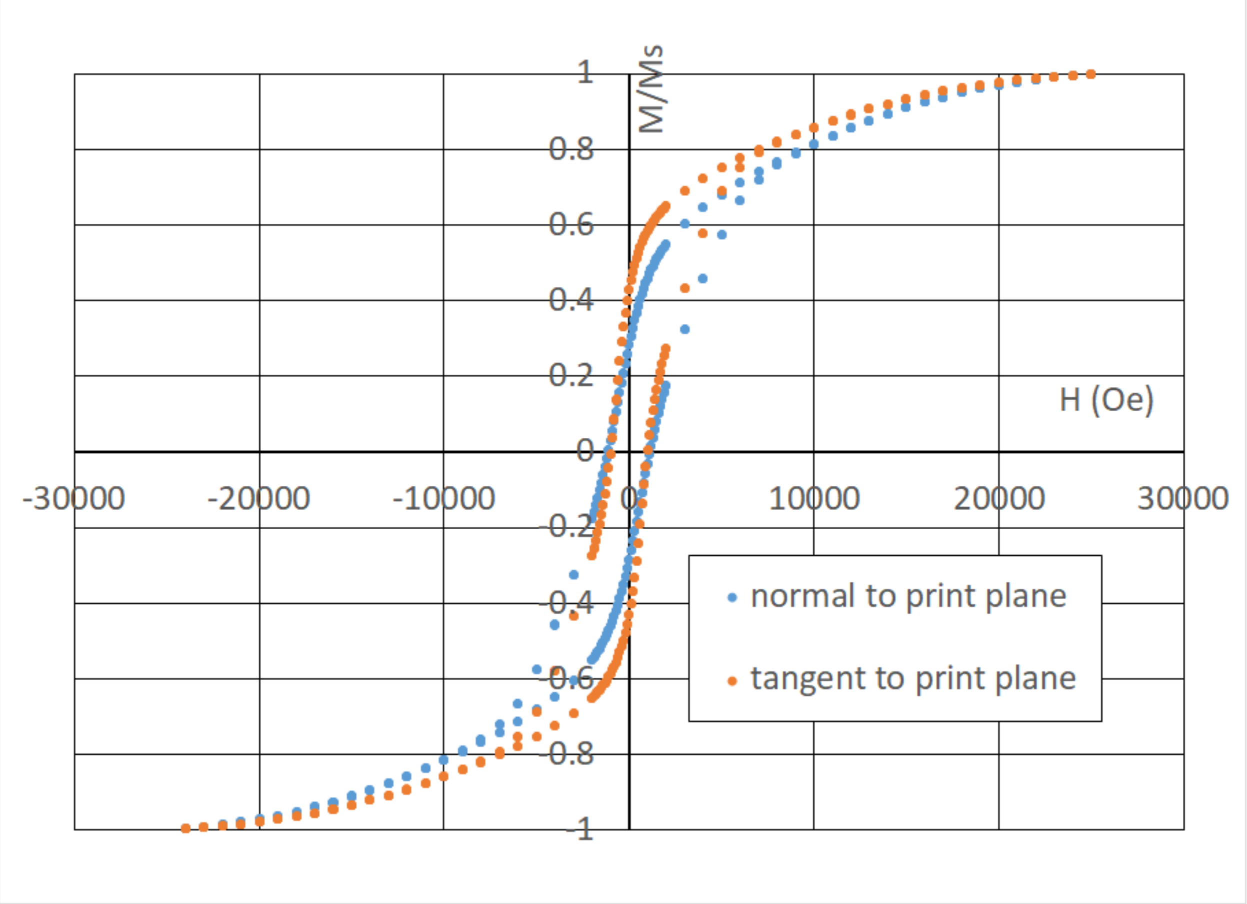

Figure 51 MH curves of In-plane in-situ poling of 5% SrM-SU8 2005 composite; the difference in remanence between the two axes is about 15%

The magnetic anisotropy is 15%; this is a good result comparing to the reference sample, which is about 20% in anisotropy. Though this setup does not contribute to the circulator application, it does contribute toward complete 3D poling of magnetic composite in 3D printing.

Another point of note is the coercivity of the composite. Coercivity is the external magnetic field needed to completely demagnetize the material. On the MH curves, the H-axis intercepts are the coercivity values. From Table I, the coercivity of the particles is measured at 1093 Oe, therefore, the coercivity from the SQUID/VSM measurements should be around this value. If the coercivity is significantly lower, this indicates that the particles may be rotating inside the polymer matrix, which means that the matrix is not fully cured.

Section 4.3: Ferromagnetic Resonance (FMR) Measurement

With the SQUID/VSM establishing the magnetic anisotropy of the composites, one more important requirement still has to be met for the composite to be considered as an appropriate material for circulators, ferromagnetic resonance. To measure the FMR frequency and estimate the permeability of the hexaferrite-polymer composites, shorted-end one-port setup [71], [72], as shown in Fig. 52 is used. Before the measurement, setup is calibrated with TRL (Thru-Reflect-Line) calibration method, which is a group of calibration that measures one through standard, and one reflection standard, and two transmission standards for accurate results [73]. The line standards should have length ~1/4 wavelength, or from 6% to 44% of a wavelength, of the measured wave. The reflected standard should have the exact same length as the shorter line standard. Calibration is done on the Z_{mid} plane as shown on right side of Fig. 52. Hence the effect of the adapter is eliminated.

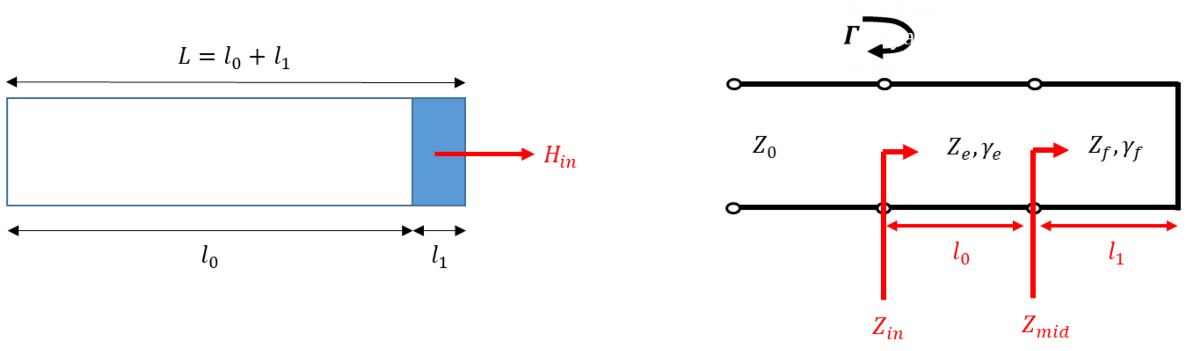

Figure 52 Measurement of FMR and permeability

The physical setup is shown in Fig. 53. First, ferrite material is fabricated in a WR19 waveguide spacer with 1.97mm thickness, as shown at the upper-right corner of in Fig.53.

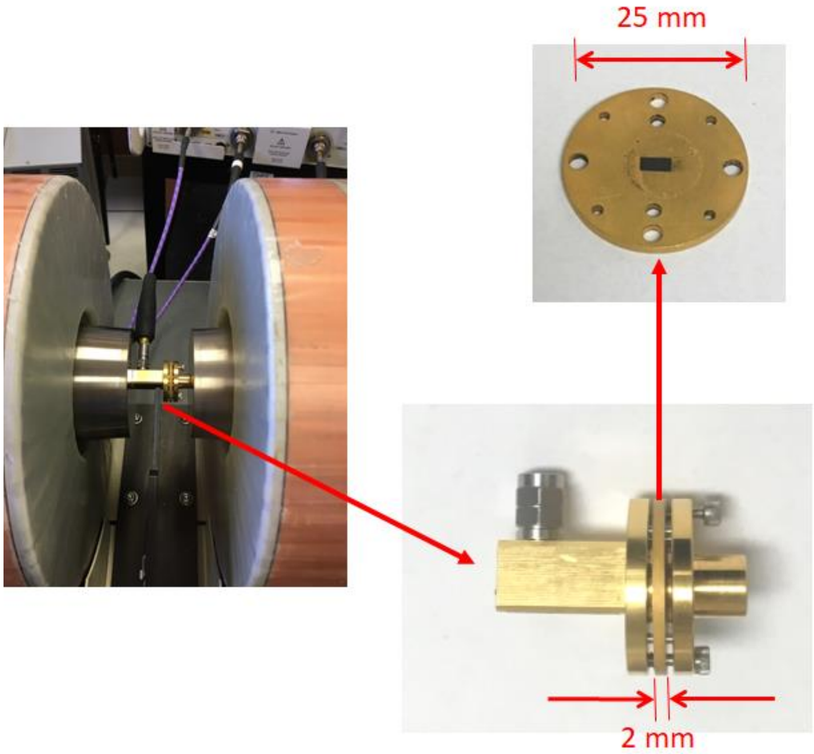

Figure 53 FMR and permeability measurement setup

Once the calibration is done, S11 is measured with a network analyzer. Then, S11 value is converted to Z_{in} by Eqn. 4-1. Since the system is calibrated on the Z_{mid} plane $Z_{in}=Z_{mid}$.

$$Z_{mid} = 50\Omega\frac{1+S_{11}}{1-S_{11}} \tag{4-1}$$

For a short ended lossy waveguide

$$Z_{mid} = Z_f tanh\left(\gamma_f l_1\right) \tag{4-2}$$

where Z_f and γ are the wave impedance and propagation constant in the ferrite filled waveguide, respectively. By substituting

$$Z_f = \frac{i\omega\mu_0\mu_r}{\sqrt{\left(\frac{\pi}{a}\right)^2 + \omega^2\mu_0\varepsilon_0\mu_r\varepsilon_r}} \quad and \quad \gamma = \sqrt{\left(\frac{\pi}{a}\right)^2 + \omega^2\mu_0\varepsilon_0\mu_r\varepsilon_r}$$

into Eqn. 4-2 we can obtain Eqn. 4-3

$$\frac{i\omega\mu_0\mu_r}{\sqrt{\left(\frac{\pi}{a}\right)^2 + \omega^2\mu_0\varepsilon_0\mu_r\varepsilon_r}} tanh\left(\sqrt{\left(\frac{\pi}{a}\right)^2 + \omega^2\mu_0\varepsilon_0\mu_r\varepsilon_r}\; l_1\right) - Z_{mid} = 0 \qquad (4\text{-}3)$$

Then Eqn. 4-3 is solved numerically for $\mu_r\varepsilon_r$. If permittivity of the material is known, μ_r can be calculated. Most of the theoretical and experimental work of FMR and permeability is done my collaborators, Dr. Umut Tok, Srinivas Prasad, and Prof. Yuanxun Wang. Representative results are selected and shown here. The FMR frequency of a 5% strontium hexaferrite-SU8-2005 composite is measured, and two more samples, a 10% strontium hexaferrite-SU8-2000.5 and a 20% strontium hexaferrite-SU8-2000.5 composite samples are measured as well for comparison. The results are shown in Fig. 54. In the absence of an external magnetic field, the FMR is around 47 GHz due to the high internal magnetic field from MCA. This value is close to the theoretical values, 56 GHz is the particles are mostly spherical or 51 GHz if mostly disc-like. There are a couple notable features in the comparison of the 5% to the 10% and 20% composite. First, the FMR frequency in all three samples increases as the bias field increases. This is expected from the Kittel's equation, shown in the Chapter 2. As the bias increases in the direction of the MCA direction, the frequency would also increase because it effectively increases the total applied field according to the equation. Second, the 5% sample seems to have a higher FMR frequency comparing to the other two samples, which have the frequency at ~43 GHz. This is a more subtle effect; the hypothesis for the phenomenon is that the closer distance between hexaferrite particles in the higher concentration samples could lead to the magnetic field from every hexaferrite particle interfering with one another. The interference leads to effectively lower the field from MCA. However, this hypothesis needs more modeling and simulation to be verified.

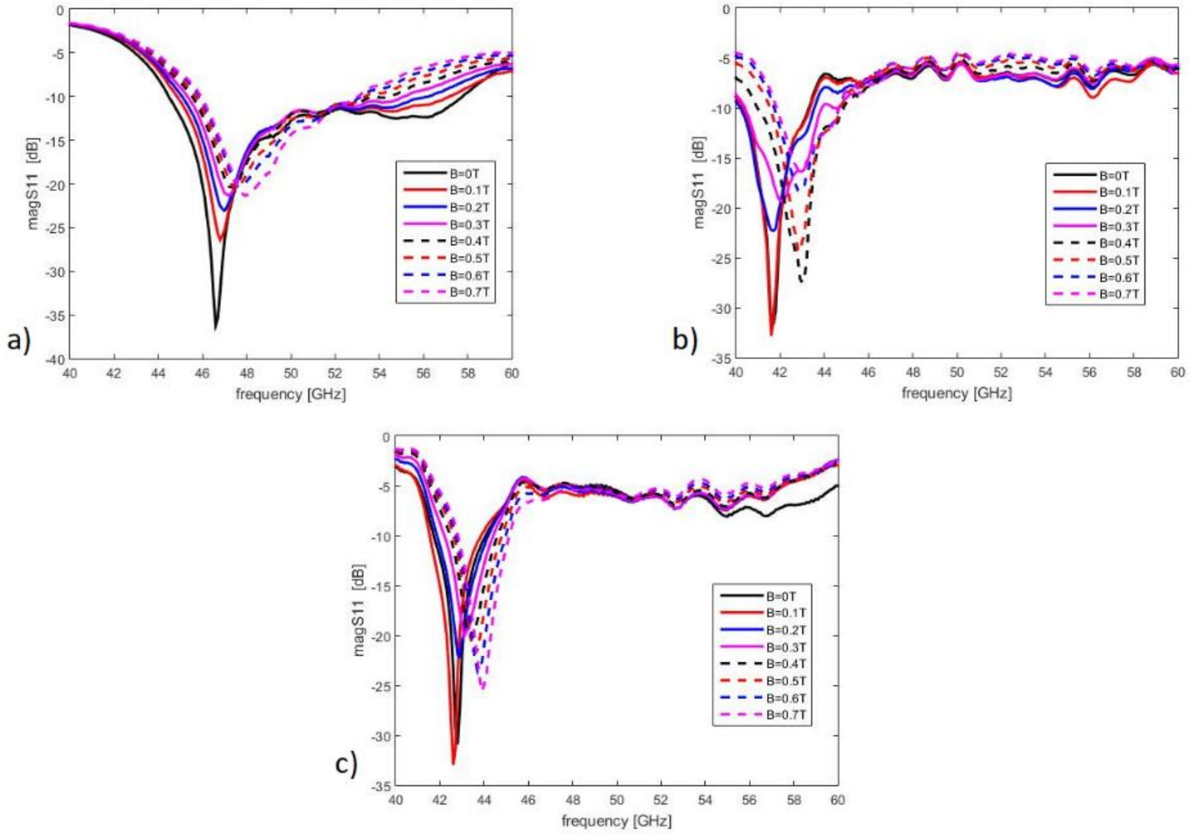

Figure 54 FMR Response of a) 5% SrM-SU8 2005, b) 10% SrM-SU8 2000.5, and c) 20% SrM-SU8 2000.5; a common feature among the 3 composites is that all of them showed FMR at 0 external bias. This is the evidence of self-bias of strontium hexaferrite

Section 4.4: Magnetic Force Microscopy

Magnetic force microscopy (MFM) is a type of scanning probe microscopy, in which a sharp magnetized probe scans a magnetic sample. The magnetic interaction between probe tip and the sample is detected and used to reconstruct the magnetic structure of the sample surface. MFM can be conducted in junction with atomic force microscopy (AFM) so both the surface topography and magnetic structure can be imaged. Fig. 55 shows a schematic of the MFM scanning surfaces with different magnetization direction. The force acting and thus affecting the scanning probe can be calculated in this equation: $\vec{F} = \mu_0(\vec{m} \cdot \nabla)\vec{H}$. An easier way to qualitatively illustrate the effect is to imagine two magnets have poles facing each other in a line versus poles orthogonal to one another. The former case would have a much stronger reaction than the later. This is the case when a poled sample surface is scanned in MFM in two orthogonal directions. As Fig. 56 shows, the contrast is much larger when the probe is scanning in the poled direction compared to the orthogonal direction. This image further illustrates the magnetic anisotropy in the poled composite.

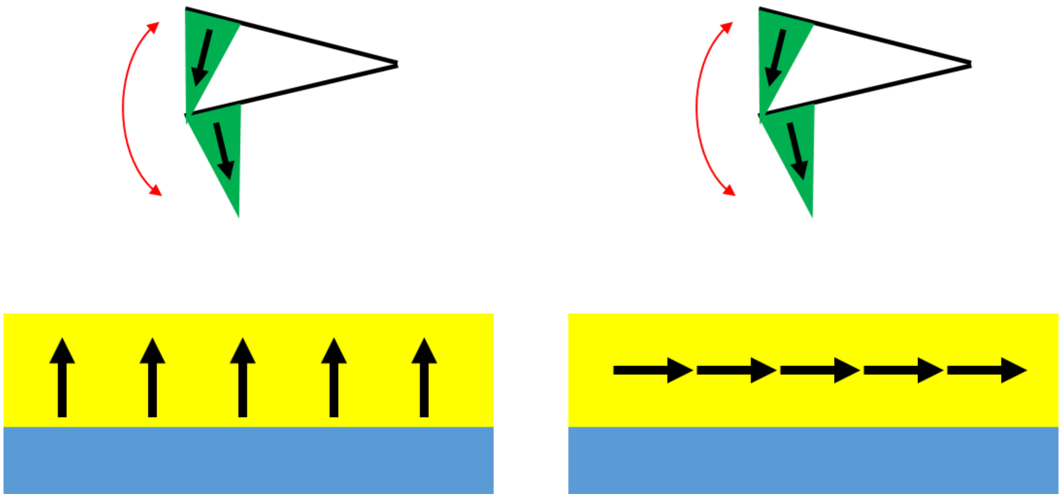

Figure 55 Magnetized tip scanning sample with out-of-plane magnetization (left) vs. sample with in-plane magnetization (right)

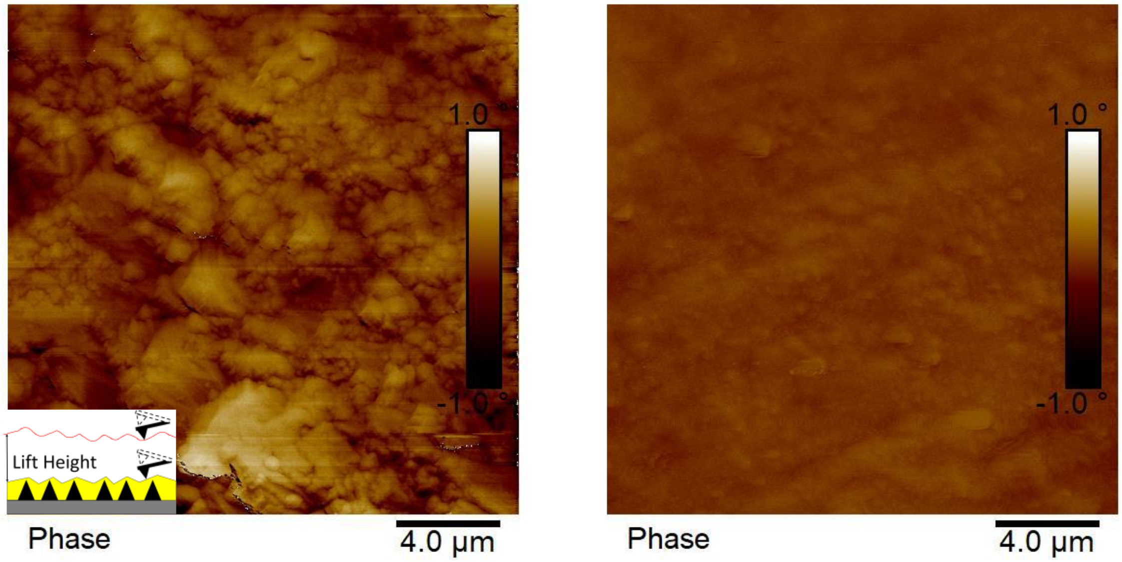

Figure 56 The MFM image on the left was measured in the poled direction, and the image on the right was measured 90° to the poled direction. The phases are shown in the same scale, from 1° to -1°. As expected, the contrast is much stronger in the poled direction, as shown on the left image. The inset on the bottom left shows the schematic of the MFM methodology.

Chapter 5: Conclusion

Section 5.1: Summary and Conclusion

The motivation of the study is the monolithic integration of hexaferrite on semiconductor substrates for circulator application. The proposed solution and also the goal of this study is to create a composite of hexaferrite particles and polymer that can be used by a 3D printer of FDM/FFF type to directly deposit the composite onto a semiconductor substrate and subsequently pole it. The composite should overcome the incompatibility arise from the different lattices of the two materials. Since this composite is meant to fabricate circulators and isolators of millimeter wave band, it must exhibit FMR in 30-300 GHz and be poled so the magnetization of the composite is perpendicular to the substrate. Due to strong magnetocrystalline anisotropy (MCA) associated with hexaferrite materials, a set of conditions, including shape of hexaferrite particles and viscosity of polymer, must be met.

Using spherical strontium hexaferrite particles and SU-8 photoresist as polymer matrix, the composites of the two materials were made and tested. Different volume concentration of strontium hexaferrite, from 1% to 20%, showed out-of-plane magnetic anisotropy after post-printing poling. Starting from as low as 10%, the surface of the deposited composite turns spikey when it is poled post printing. The spiking of the surface is most likely caused by the strong self-interaction among hexaferrite particles. The spikey surface is undesirable because it can lead to additional processing for making circulators and thus limit the highest volume concentration that can be used. However, if the volume concentration of strontium hexaferrite is too low, then FMR response would be too low to be measured. With the volume concentration lowered to 5%, the composite of strontium hexaferrite in SU-8 2005 showed no spiking while poled post printing while meeting all the other requirements and exhibit FMR at ~43-44 GHz under bias 0-0.7T.

Section 5.2: Future Work on Improving 3D Printing Magnetic Composites

Though the goal of 3D printing and poling a magnetic composite was met using a particular combination of hexaferrite particles and liquid polymer, there is always room for improvement. One of possibilities is to have spherical particles of strontium hexaferrite with smaller diameters. The ideal size would be about 1 um, which is close to the size of single domain [67]. The closer to single domain a hexaferrite particle is, the higher its remanent magnetization would be, which would lead to a higher torque for rotation in the presence of an external magnetic field. With single-domain hexaferrite particles, the squareness ratio, remanent magnetization divided by saturation magnetization, of the particles should increase, which should lead to higher magnetic anisotropy of the composite. Another possibility is that the polymer matrix can be replaced with something that has less solvent content and high storage modulus so there is less volume and shape change after the polymer cures [14]. To simplify the curing process, the polymer could be cured chemically with a hardener or heat (at temperature compatible with other electrical components or process steps) as demonstrated in other works [74].

In-situ poling can also be implemented on the print head, as it was for in-plane orientation. The original idea was to use electromagnets for poling because they provide more control as compared to permanent magnets. However, the initial design show too much heat generated as over 1 A of current goes through the coil for version of coils used. If current is decreased, not enough magnetic field can be generated to pole the hexaferrite composite. Permanent magnets could be used to bypass the overheating issue and provide higher field strength. A magnetic flux guide needs to be fabricated to make the out-of-plane in-situ poling device. More designing and simulation is needed to estimate the heat generated from using electromagnets on poling devices. It would be more beneficial to use electromagnets in in-situ poling setups so the magnetization directions within a printed sample can be changed at will. A conceptual schematic of the in-situ out-of-plane poling is shown in Fig. 25 and with more details in Fig. 57. A schematic of the in-situ in-plane poling is shown in Fig. 24; which uses the same idea of electromagnet.

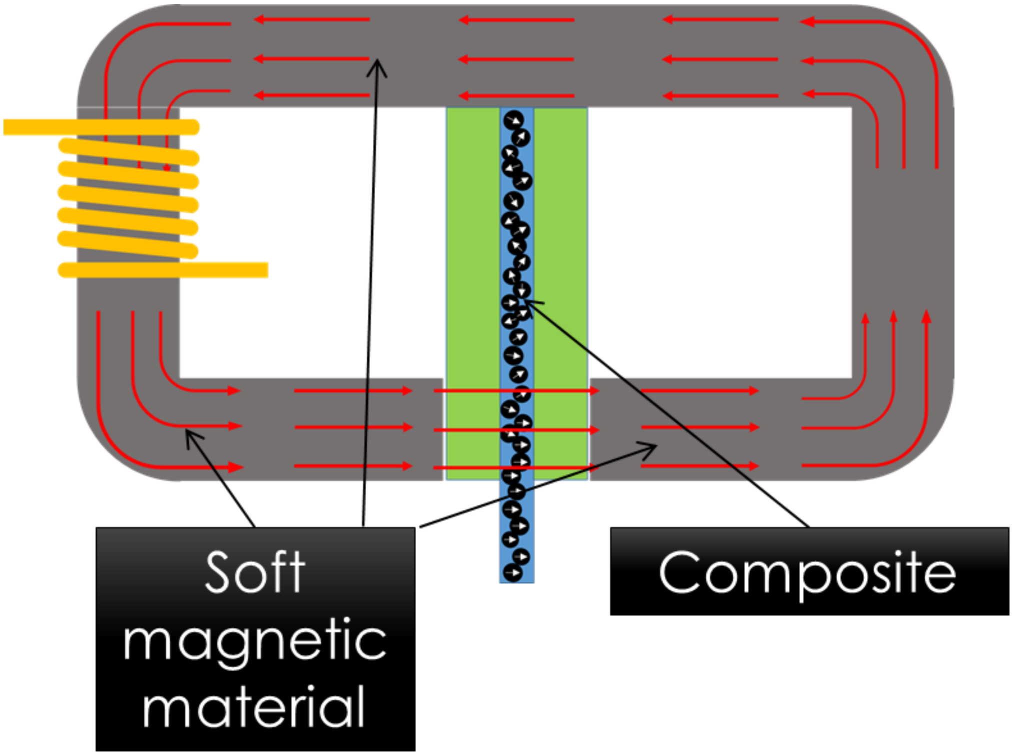

Figure 57 Future in-situ out-of-plane poling setup

After the hardware of in-situ poling is incorporated onto the printer, some modification will still be needed to control the poling setup. Controlling the poling setup includes turning it on and off in sync with the printing and changing the poling direction. To achieve this goal, custom modification in both hardware and software need to be implemented. One example of a complex magnetic device suitable for 3D printing is a magnetic quadrupole, with magnetic domains arranged in Halbach array fashion, like the one shown in Fig. 58.

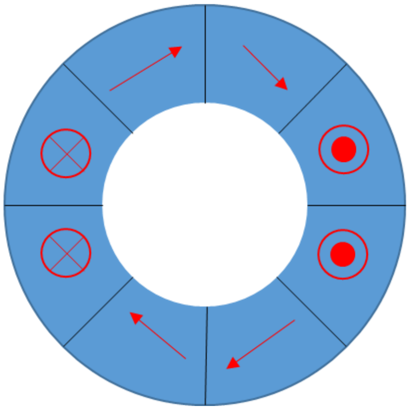

Figure 58 A Halbach array-like structure

This technique of 3D printing with a composite of magnetic material in a polymer matrix has a broader range of application beyond just millimeter-wave magnetic devices. Either the magnetic material or the polymer matrix can be changed to different varieties, depending on the application. For example, the magnetic particles can be made of NdFeB, which would have very high magnetization and suitable for low-frequency applications. The polymer matrix can also be changed from SU8 to silicone-based polymer or PDMS, which is not photosensitive. As long as the composite meets the requirements outlined in Chapter 2, it can used in a 3D printer of FDM/FFF-type.

Section 5.3: Future Outlook and Additional Applications

Moving beyond the circulator and MM-wave applications, the technique of 3D printing composite materials can be applied to many other fields. Another application for this type of material is inductor, which benefits from increased permeability. Past studies have been performed to make this type of composite and 3D printed for this purpose as well [17]. Fig. 59 shows the work done by Han Song *et al.* [17] for possible inductor applications. The aligned sample shows higher permeability at high frequency (1-3 GHz) and thus leads to higher inductance.

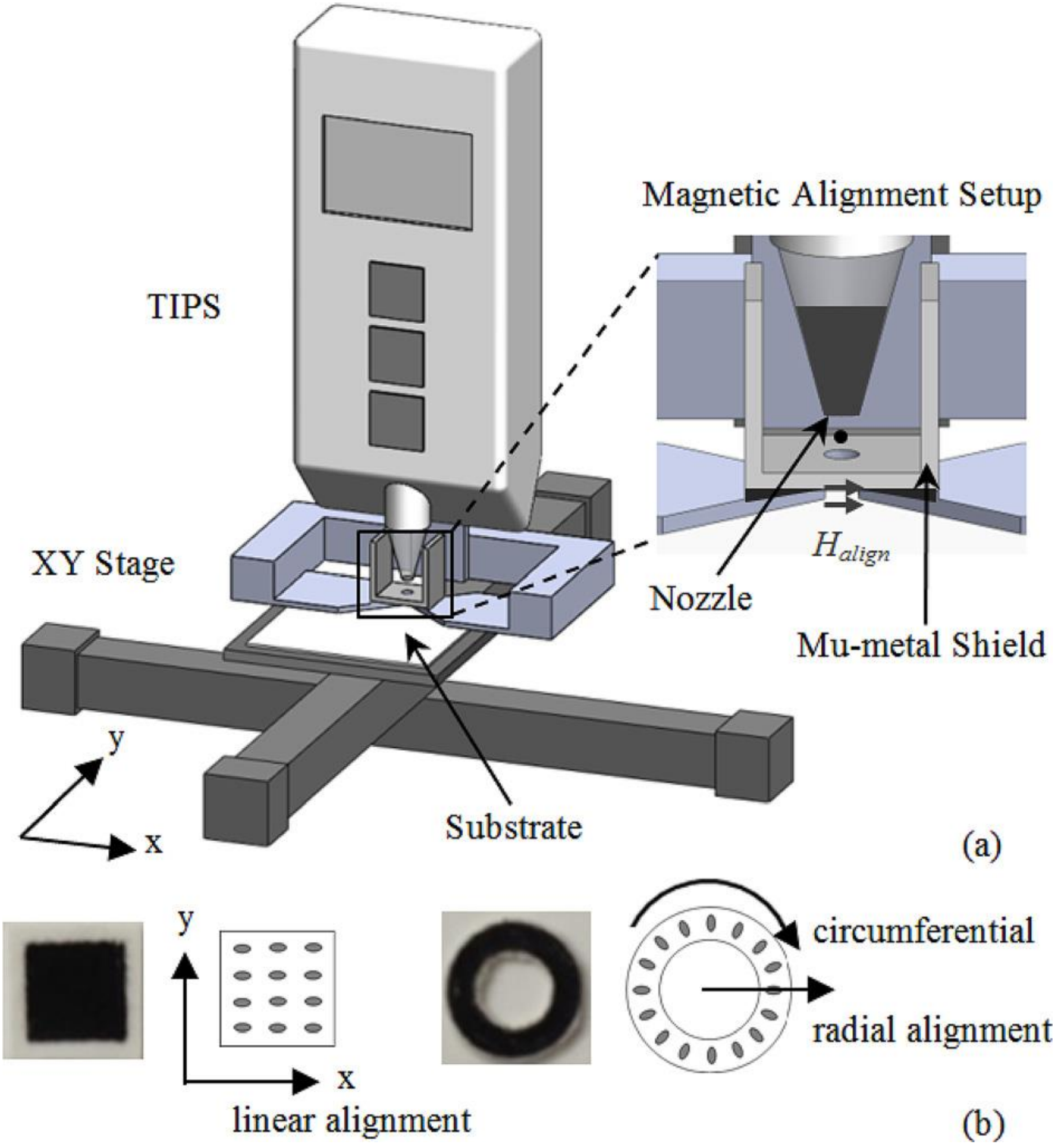

Figure 59 (a) Schematic of inkjet printing and magnetic alignment setup. (b) Photos and schematics of x direction aligned square sample and radial direction aligned ring shaped sample [17].

In the appendix, an example of printing magnetically isotropic filament is shown. This type material is already shown to be suitable for making rotary pumps in study done by Kai von Petersdorff-Campen *et al.* [56]. A working example was made, as shown in Fig. 60. Using 3D printing or additive manufacturing in general overcomes the bottleneck in conventional magnet manufacturing is a significant bottleneck in the development, which is the long lead times requires for every iteration of design adaption requires. The technique also gives new possibilities for complex designs, which could be economically unfeasible in conventional fabrication.

Figure 60 Fully printed pump with drive unit after removal of support material (no magnets visible, coated with silicone)[56] .

Aside from using magnetic composites for their magnetic characteristics in electromagnetic applications, poling the magnetic components inside the composites can be used for modifying their mechanical and structural properties. An example is poling magnetic fibers inside a magnetic composite to enhance the strength in one direction, or anisotropy in modulus [74], [75]. Fig. 61 shows the work done Joshua Martin *et al.* [74]; the magnetic fibers rotate into the direction of the external magnetic field and thus modify the modulus.

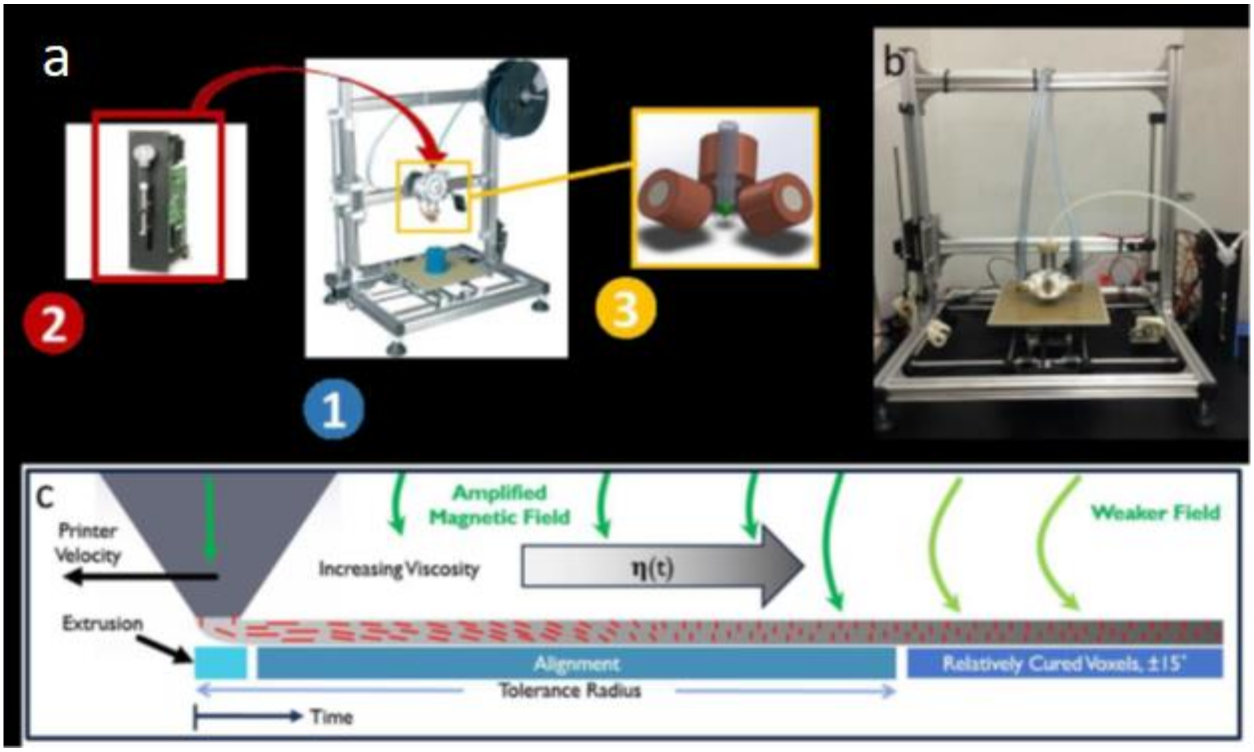

Figure 61 a) Overview and b)actual image of the final magnetic direct-write printer used in this work. This printer is capable of extruding fiber reinforced composite precursor solution and subjecting the extrudite to magnetic field in real-time to orient the magnetically active reinforcing particles in an epoxy matrix before it cures. c) Overview image of the real-time orientation requirements of magnetically active reinforcing particles in a curing epoxy matrix. As the particles are extruded from the syringe tip they are shear aligned along the printing direction. Before the epoxy cures, the particles need to be oriented with the magnetic field [74].

Similar study is done by Luquan Ren *et al.* [76], shown in Fig. 62. The composite used in this work is a combination of resin and steel fibers. The steel fibers rotate in the direction of the magnetic field provided by the permanent magnet mounted on the stage of the printer. With the directed fibers in the composite, the printed structure would have different mechanical responses or displacement under different stimuli.

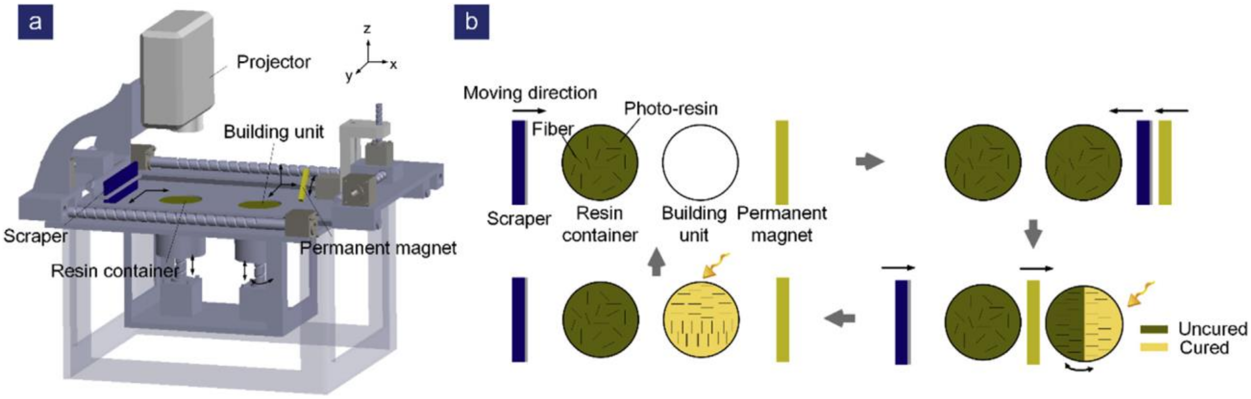

Figure 62 3D printing of shape memory stripes with aligned fibers. (a) Schematic of the magnetic assembly and modified slurry-based stereolithography 3D printer. (b) Diagram of the 3D printing process [76].

Yet another example is using softer polymer, such as hydrogel, as the matrix of the magnetic composite [77]. The composite can be used as the basis to build soft robots, as shown in Fig. 63. If the hydrogen gel is biocompatible, it could be the basis of micro scale robots and devices that are meant for biomedical applications.

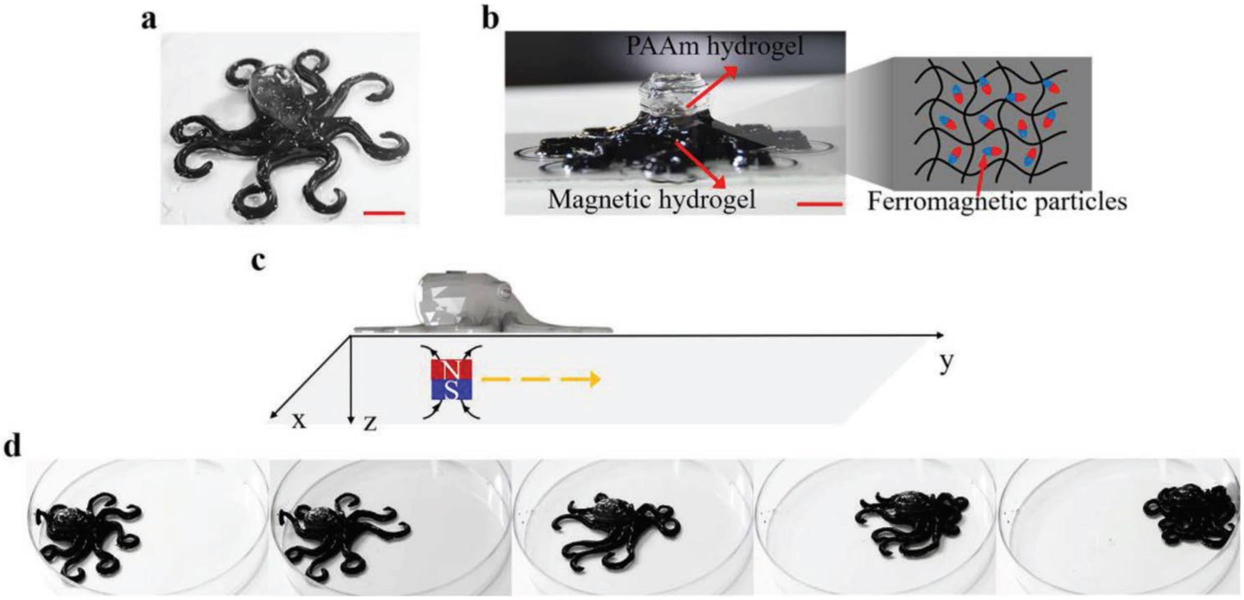

Figure 63 a) 3D printing of a soft octopus robot of hydrogels. b) Front view of octopus robot which is fabricated by two parts: 1) hydrogel is used to print the transparent head; 2) hydrogel mixed with ferromagnetic particles (Fe_3O_4) is used to print the tentacles for achieving motions under magnetic field. c) Schematics of the octopus robot moving under the driving of a magnetic field on the "x–y" plane. d) The octopus robot achieves a forward movement when the magnetic field is programmed to move from left to right. (Scale bars, 1 mm.) [77]

Through the examples given above, the potential of magnetic 3D printing should become obvious. Using the same concept, the composite can even respond to other stimuli such as electrical field or light. Not only can the composite introduce new properties to the material over, it can even have varying properties depending on the changing conditions. With the combination of composite materials and additive manufacturing, the technique also makes the fabrication of meta-materials much easier and opens up many new paths to different kinds of applications. Comparing to conventional manufacturing and fabrication, the relative low cost also makes it friendly to research and development for small companies.

Appendix: 3D Printing Magnetically Isotropic Composite

Section A.1: Other Magnetic Composite

As it was discussed in the overview of 3D printing, the FDM/FFF type of 3D printer can use either a thermoplastic or other type of filament. A class of material known as magnetorheological elastomer has been studied. Other magnetic and non-magnetic composites have been 3D printed as well for different purpose [75]–[79]. The field and technique was pioneered by J. Lewis and company over a decade ago [14], [15], [58], [61]. The versatility of the technique allows any other combination of magnetic material and polymer matrix. This body of work focused on hexaferrite particles; however, any other type of ferro- or ferrimagnetic material can be used. Similarly, the study thus far has described a liquid photoresist; however, any other type of polymer can be used as long as it can meet the first three requirements described in Section 2.5. An original example described in the following section illustrates the point.

Section A.2: Example of Hexaferrite-thermoplastic Composite

If magnetic anisotropy is not needed (e.g. printing an inductor or motor) for the composite, then there will be no need for poling. The magnetic material can be isotropic magnetically. The polymer matrix, as a result, can have high viscosity, or even solid, for the ease of extrusion. There are several thermoplastic materials that are common for monolithic filaments; a couple common ones are acrylonitrile butadiene styrene (ABS) and polylactic acid (PLA). These materials are selected as the example because they can be dissolved by solvents of relatively low toxicity. ABS can be dissolved by acetone, and PLA can be dissolved by dichloromethane. The magnetic particles can be mixed uniformly in the dissolved and liquid state polymer with a centripetal mixer like Think AR-100. Such a mixture is shown in Fig. 64. This approach has been studied and tried in prior art [78], [80].

Figure 64 Mixture of dissolved ABS and barium hexaferrite particles.

After the mixture, or sol-gel, is made, it needs to be heated to evaporate the solvent. The solvents mentioned have low boiling point so they can be baked rather safely, and the mixture becomes solid. The solid composite is shown in Fig. 65; the composite in turn can be crushed into smaller pieces and fed into a filament extruder. If both the polymer and magnetic material are in particle form, they can also be mixed together and extruded to form filament directly. An example of such extruded filament is shown in Fig. 66.

Figure 65 Dried mixture of ABS and hexaferrite particles.

Figure 66 SrM and ethylene ethyl acrylate (EEA) polymer extruded filament[11]*; filaments similar to this was made with BaM and ABS/PLA*

Since magnetic anisotropy is not a requirement for the filament, it can be used to print like a monolithic thermoplastic one without any additional modification to an FDM/FFF 3D printer. Since the polymer matrix used is not magnetic, the saturation magnetization of the composite typically follows the equation below:

$$\%_{volume} * M_{s(magnetic\ particles)} = M_{s(composite)} \quad \text{(A-1)}$$

Filaments of barium hexaferrite ($BaFe_{12}O_{19}$) and ABS/PLA composites were made with different barium hexaferrite concentration. The filaments were tested in the SQUID/VSM, and results are shown in Fig. 67.

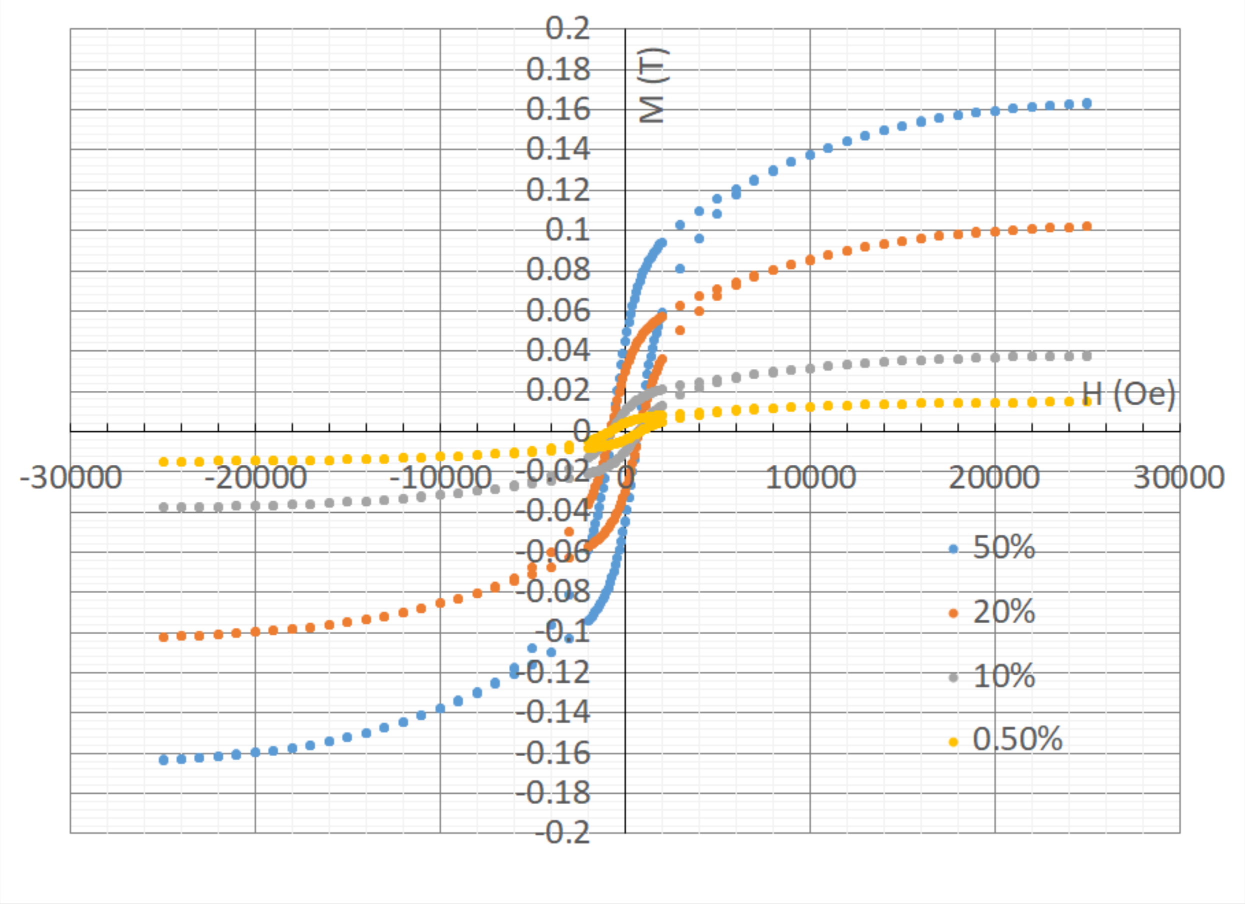

Figure 67 Filaments made with different volume concertation of BaM. The 0.5% and 10% samples are made with PLA, and the other two are made with ABS.

Considering the saturation magnetization (M_s) of barium hexaferrite to be about 0.37 Tesla [81], the graphs shown demonstrates the saturation magnetization measured in different filaments follow the Eqn. A-1 well with the exception of 0.5% filament. The deviation of remanence of the 0.5% filament from the equation is mostly likely due to the limit of the resolution of the mass measurement for low amount of hexaferrite material. If the measurements from Fig. 60 are normalized to the volumes of the hexaferrite particles, then the graphs from all the filaments become almost identical as shown in Fig. 68.

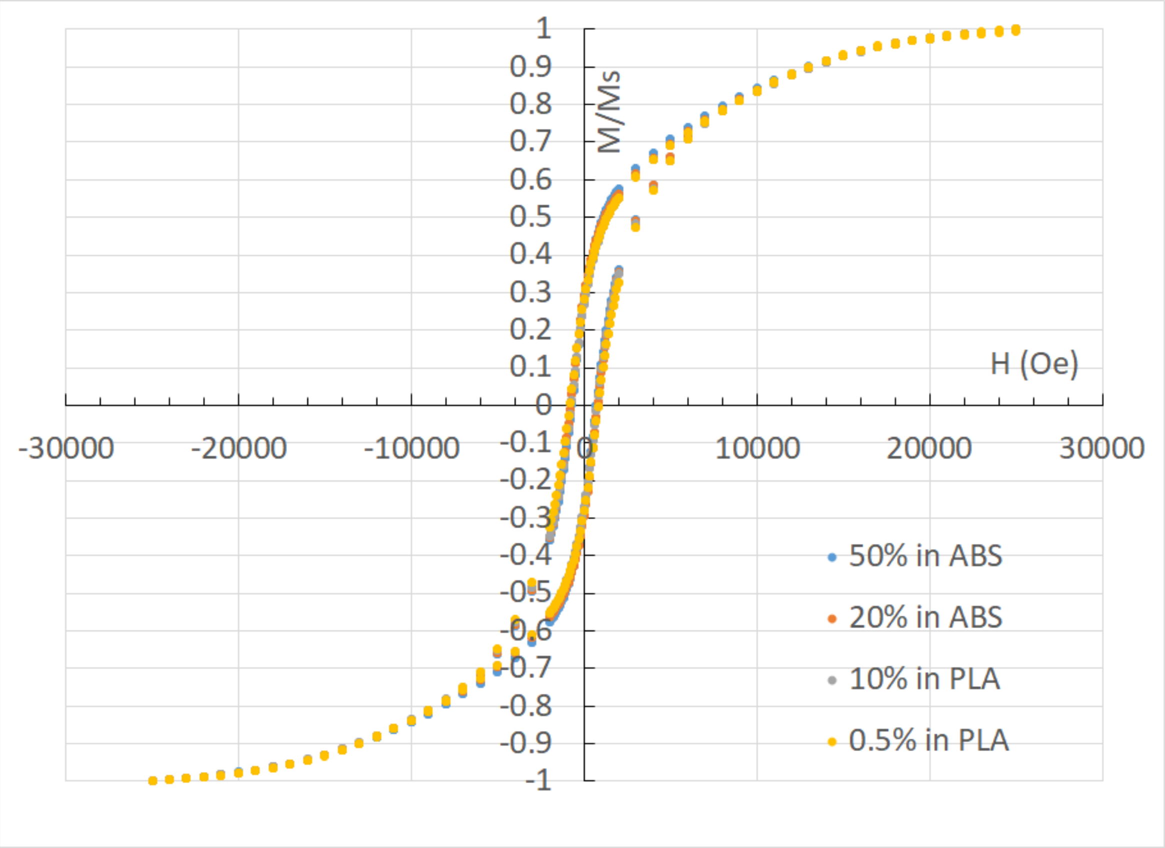

Figure 68 The measurements in Fig. 67 normalized to the volumes of BaM particles in every sample.

The convergence indicates that the polymer is not contributing to the magnetic behavior of the filament, which is expected. It also indicates that the particles are all randomly oriented in across all the filaments of different BaM concentration. Since the filaments were not poled before the measurement, the orientation should be random and thus gives the same net MH curves. This also indicates that the magnetization should be isotropic.

Reference

[1] D. T. Jangam, “Mm Waves Role in Satellite Communication,” *IOSR J. Electron. Commun. Eng.*, vol. 4, no. 4, pp. 1–4, 2013.

[2] P. R. Rao, “Role of MM Waves In Terrestrial and Satellite Communications,” *Int. J. Syst. Technol.*, vol. 3, no. 1, pp. 25–34, 2010.

[3] C. Cox and E. Ackerman, “Demonstration of a single-aperture, full-duplex communication system,” *IEEE Radio Wirel. Symp. RWS*, pp. 148–150, 2013.

[4] U. Editor, “Transmit/Receive Modules.” [Online]. Available: https://www.microwaves101.com/encyclopedias/transmit-receive-modules.

[5] T. Fitchorov and A. Geiler, “Miniaturized, Low-cost, Self-biased Circulators for Space and Airborne Applications,” in *Earch Science Technology Forum 2016*, 2016.

[6] C. Kärnfelt, R. Kozhuharov, and H. Zirath, “Multipliers in pHEMT and mHEMT Technology,” vol. 54, no. 6, pp. 15–20, 2006.

[7] P. C. Dorsey, D. B. Chrisey, J. S. Horwitz, P. Lubitz, and R. C. Y. Auyeung, “Oriented barium hexaferrite thick films grown on c-plane and m-plane sapphire substrates,” vol. 30, no. 6, pp. 4512–4517, 1994.

[8] X. Wang, M. Jiang, Z. Zhou, J. Gou, and D. Hui, “3D printing of polymer matrix composites: A review and prospective,” *Compos. Part B Eng.*, vol. 110, pp. 442–458, 2017.

[9] L. Li *et al.*, “Big Area Additive Manufacturing of High Performance Bonded NdFeB Magnets,” *Sci. Rep.*, vol. 6, no. October, pp. 1–7, 2016.

[10] C. Huber *et al.*, “3D print of polymer bonded rare-earth magnets, and 3D magnetic field

scanning with an end-user 3D printer," *Appl. Phys. Lett.*, vol. 109, no. 16, pp. 1–5, 2016.

[11] E. M. Palmero, D. Casaleiz, N. A. Jiménez, and J. Rial, "Magnetic-Polymer Composites for Bonding and 3D Printing of Permanent Magnets," pp. 1–4, 2018.

[12] P. Von Lockette, S. E. Lofland, J. Biggs, J. Roche, J. Mineroff, and M. Babcock, "Investigating new symmetry classes in magnetorheological elastomers: Cantilever bending behavior," *Smart Mater. Struct.*, vol. 20, no. 10, 2011.

[13] A. K. Bastola, V. T. Hoang, and L. Li, "A novel hybrid magnetorheological elastomer developed by 3D printing," *Mater. Des.*, vol. 114, pp. 391–397, 2017.

[14] J. A. Lewis, "Direct ink writing of 3D functional materials," *Adv. Funct. Mater.*, vol. 16, no. 17, pp. 2193–2204, 2006.

[15] J. E. Smay, J. Cesarano, and J. A. Lewis, "Colloidal inks for directed assembly of 3-D periodic structures," *Langmuir*, vol. 18, no. 14, pp. 5429–5437, 2002.

[16] Y. Kim, H. Yuk, R. Zhao, S. A. Chester, and X. Zhao, "Printing ferromagnetic domains for untethered fast-transorming soft materials," *Nature*, vol. 558, no. 7709AB, p. Supp. 1-7, 2018.

[17] H. Song *et al.*, "Inkjet printing of magnetic materials with aligned anisotropy," *J. Appl. Phys.*, vol. 115, no. 17, p. 17E308, 2014.

[18] V. G. Harris *et al.*, "Ba-hexaferrite films for next generation microwave devices (invited)," *J. Appl. Phys.*, vol. 99, no. 8, pp. 1–5, 2006.

[19] P. Shi, H. How, X. Zuo, S. D. Yoon, S. A. Oliver, and C. Vittoria, "MMIC circulators using hexaferrites," *IEEE Trans. Magn.*, vol. 37, no. 4 I, pp. 2389–2391, 2001.

[20] F. K. H. Gellersen and A. F. Jacob, "A sol-gel approach for self-biased barium hexaferrite

thin-film circulators," *Eur. Microw. Week 2016 "Microwaves Everywhere", EuMW 2016 - Conf. Proceedings; 46th Eur. Microw. Conf. EuMC 2016*, pp. 361–364, 2016.

[21] L. Chao, H. Oukacha, E. Fu, V. J. Koomson, and M. N. Afsar, "Millimeter wave complementary metal-oxide-semiconductor on-chip hexagonal nano-ferrite circulator," *J. Appl. Phys.*, vol. 117, no. 17, 2015.

[22] A. Morisako, X. Liu, M. Matsumoto, and M. Naoe, "The effect of underlayer for Ba-ferrite sputtered films on c-axis orientation," *J. Appl. Phys.*, vol. 81, no. 8, pp. 4374–4376, 2002.

[23] E. Lacroix, P. Gerard, G. Marest, and M. Dupuy, "Substrate effects on the crystalline orientation of barium hexaferrite films," *J. Appl. Phys.*, vol. 69, no. 8, pp. 4770–4772, 1991.

[24] S. R. Shinde *et al.*, "Realization of epitaxial barium ferrite films of high crystalline quality with small resonance losses," *J. Appl. Phys.*, vol. 85, no. 10, pp. 7459–7466, 1999.

[25] I. Wane *et al.*, "Thick barium hexaferrite (Ba-M) films prepared by electron-beam evaporation for microwave application," *J. Magn. Magn. Mater.*, vol. 211, no. 1, pp. 309–313, 2000.

[26] Y. Gao, Y. J. Kim, S. Thevutasan, S. A. Chambers, and P. Lubitz, "Growth, structure, and magnetic properties of γ-Fe2O3 epitaxial films on MgO," *J. Appl. Phys.*, vol. 81, no. 7, pp. 3253–3256, 1997.

[27] S. D. Yoon, C. Vittoria, and S. A. Oliver, "Magnetization behavior of scandium-substituted barium hexaferrite films having uniaxial axis in the film plane," *J. Magn. Magn. Mater.*, 2003.

[28] Z. Chen and V. G. Harris, "Ferrite film growth on semiconductor substrates towards microwave and millimeter wave integrated circuits," *J. Appl. Phys.*, vol. 112, no. 8, 2012.

[29] H. Arnold *et al.*, *International Tables for Crystallography Volume A: Space-group symmetry*, 5th ed. Springer-Verlag, 2002.

[30] X. Zhang, S. Meng, D. Song, Y. Zhang, Z. Yue, and V. G. Harris, “Epitaxially grown BaM hexaferrite films having uniaxial axis in the film plane for self-biased devices,” *Sci. Rep.*, vol. 7, no. February, pp. 1–9, 2017.

[31] L. Chao, O. Sholiyi, M. N. Afsar, and J. D. Williams, “Characterization of micro-structured ferrite materials: Coarse and fine barium, and photoresist composites,” *IEEE Trans. Magn.*, vol. 49, no. 7, pp. 4319–4322, 2013.

[32] Y. Chen, A. L. Geiler, T. Sakai, S. D. Yoon, C. Vittoria, and V. G. Harris, “Microwave and magnetic properties of self-biased barium hexaferrite screen printed thick films,” *J. Appl. Phys.*, vol. 99, no. 8, pp. 2006–2008, 2006.

[33] Y. Chen *et al.*, “Realization of hexagonal barium ferrite thick films on Si substrates using a screen printing technique,” *J. Phys. D. Appl. Phys.*, vol. 41, no. 9, 2008.

[34] J. J. Went, G. W. Rathenau, E. W. Gorter, and G. W. van Oosterhout, “Ferroxdure, a class of new permanent magnet materials,” *Philips Tech. Rev.*, vol. 13, no. 7, pp. 194–208, 1952.

[35] J. J. Went, G. W. Rathenau, E. W. Gorter, and G. W. Van Oosterhout, “Hexagonal iron-oxide compounds as permanent-magnet materials,” *Phys. Rev.*, vol. 86, no. 3, pp. 424–425, 1952.

[36] J. L. Snoek, “Gyromagnetic resonance in ferrites,” *Nature*, vol. 160, no. 4055. p. 90, 1947.

[37] J. L. Snoek, “Dispersion and absorption in magnetic ferrites at frequencies above one Mc/s,” *Physica*, vol. 14, no. 4, pp. 207–217, 1948.

[38] M. Sugimoto, “Properties of ferroxplana-type hexagonal ferrites,” *Handbook of Ferromagnetic Materials*. 1982.

[39] Ü. Özgür, Y. Alivov, and H. Morkoç, *Microwave ferrites, part 1: Fundamental properties*, vol. 20, no. 9. 2009.

[40] H. N. Chait and T. R. Curry, “Y Circulator,” *J. Appl. Phys.*, vol. 30, no. 4, pp. S152–S153, 1959.

[41] D. M. Pozar, *Microwave Engineering, 4th Edition*. 2012.

[42] V. G. Harris, “Modern microwave ferrites,” *IEEE Trans. Magn.*, vol. 48, no. 3, pp. 1075–1104, 2012.

[43] “Transverse Mode.” [Online]. Available: https://en.wikipedia.org/wiki/Transverse_mode.

[44] G. B. Jeffery and L. N. G. Filon, “The motion of ellipsoidal particles immersed in a viscous fluid,” *Proc. R. Soc. LONDON. Ser. A, Contain. Pap. A Math. Phys. CHARACTER*, vol. 102, no. 715, pp. 161–79, 1922.

[45] T. Kimura, M. Yamato, W. Koshimizu, M. Koike, and T. Kawai, “Magnetic orientation of polymer fibers in suspension,” *Langmuir*, vol. 16, no. 2, pp. 858–861, 2000.

[46] R. Bozorth, *Ferromagnetism*. 1951.

[47] W. B. Russel, “Review of the Role of Colloidal Forces in the Rheology of Suspensions,” *J. Rheol. (N. Y. N. Y).*, vol. 24, no. 3, pp. 287–317, 1980.

[48] C. G. De Kruif, E. M. F. Van Iersel, A. Vrij, and W. B. Russel, “Hard sphere colloidal dispersions: Viscosity as a function of shear rate and volume fraction,” *J. Chem. Phys.*, vol. 83, no. 9, pp. 4717–4725, 1985.

[49] J. C. van der Werff and C. G. de Kruif, “Hard-sphere Colloidal Dispersions: The Scaling of

Rheological Properties with Particle Size, Volume Fraction, and Shear Rate," *J. Rheol. (N. Y. N. Y).*, vol. 33, no. 3, pp. 421–454, 1989.

[50] L. K. Lagorce and M. G. Allen, "Magnetic and mechanical properties of micromachined strontium\nferrite/polyimide composites," *J. Microelectromechanical Syst.*, vol. 6, no. 4, pp. 307–312, 1997.

[51] D. R. Saini, A. V. Shenoy, and V. M. Nadkarni, "Effect of surface treatments on rheological, mechanical and magnetic properties of ferrite-filled polymeric systems," *Polym. Eng. Sci.* , vol. 25, no. 13, pp. 807–811, 1985.

[52] P. R. von Lockette, J. Kadlowec, and J.-H. Koo, "Particle mixtures in magnetorheological elastomers (MREs)," p. 61700T, 2006.

[53] K. L. Tsai *et al.*, "Magnetic, mechanical, and optical characterization of a magnetic nanoparticle-embedded polymer for microactuation," *J. Microelectromechanical Syst.*, vol. 20, no. 1, pp. 65–72, 2011.

[54] O. Sholiyi, J. Lee, and J. D. Williams, "Electromagnetic properties of photodefinable barium ferrite polymer composites," *AIP Adv.*, vol. 4, no. 7, 2014.

[55] C. Huber *et al.*, "3D Printing of Polymer-Bonded Rare-Earth Magnets with a Variable Magnetic Compound Fraction for a Predefined Stray Field," *Sci. Rep.*, vol. 7, no. 1, pp. 1–8, 2017.

[56] K. von Petersdorff-Campen *et al.*, "3D Printing of Functional Assemblies with Integrated Polymer-Bonded Magnets Demonstrated with a Prototype of a Rotary Blood Pump," *Appl. Sci.*, vol. 8, no. 8, p. 1275, 2018.

[57] V. Tohver, A. Chan, O. Sakurada, and J. A. Lewis, "Nanoparticle engineering of complex fluid behavior," *Langmuir*, vol. 17, no. 26, pp. 8414–8421, 2001.

[58] J. A. Lewis and G. M. Gratson, “Direct writing in three dimensions,” *Mater. Today*, vol. 7, no. 7, pp. 32–39, 2004.

[59] J. F. Gilchrist, A. T. Chan, E. R. Weeks, and J. A. Lewis, “Phase behavior and 3D structure of strongly attractive microsphere- nanoparticle mixtures,” *Langmuir*, vol. 21, no. 24, pp. 11040–11047, 2005.

[60] R. B. Rao, K. L. Krafcik, A. M. Morales, and J. A. Lewis, “Microfabricated deposition nozzles for direct-write assembly of three-dimensional periodic structures,” *Adv. Mater.*, vol. 17, no. 3, pp. 289–293, 2005.

[61] B. J. E. Smay, G. M. Gratson, R. F. Shepherd, J. C. Iii, and J. A. Lewis, “2002-Directed Colloid assembly of 3D periodic structures.pdf,” no. 18, pp. 1279–1283, 2002.

[62] R. Domingo-Roca, J. C. Jackson, and J. F. C. Windmill, “3D-printing polymer-based permanent magnets,” *Mater. Des.*, vol. 153, pp. 120–128, 2018.

[63] M. Weber, “Liquid-solid flow,” *Thermopedia*, 2010. [Online]. Available: http://www.thermopedia.com/content/51/.

[64] S. Mueller, E. W. Llewellin, and H. M. Mader, “The rheology of suspensions of solid particles,” *Proc. R. Soc. A Math. Phys. Eng. Sci.*, 2010.

[65] W. H. Herschel and R. Bulkley, “Konsistenzmessungen von Gummi-Benzoll??sungen,” *Kolloid-Zeitschrift*, 1926.

[66] E. C. Stoner and E. P. Wohlfarth, “A mechanism of magnetic hysteresis in heterogeneous alloys,” *IEEE Trans. Magn.*, 1991.

[67] J. Park, Y. Hong, W. Lee, S. An, J. Seo, and K.-H. Hur, “Coercivity of SrFe12O19 Hexaferrite Platelets Near Single Domain Size,” *IEEE Magn. Lett.*, vol. 6, pp. 1–3, 2015.

[68] D. Kokkinis, M. Schaffner, and A. R. Studart, “Multimaterial magnetically assisted 3D printing of composite materials,” *Nat. Commun.*, vol. 6, pp. 8643–52, 2015.

[69] R. M. Erb, R. Libanori, N. Rothfuchs, and A. R. Studart, “Composites Reinforced in Three Dimensions by Using Low Magnetic Fields,” *Science (80-.).*, vol. 202508, no. January, pp. 199–205, 2012.

[70] M. McElfresh, *Fundamentals of Magnetism and Magnetic Measurements Featuring Quantum Design’s Magnetic Property Measurement System*. Quantum Design, Inc, 1994.

[71] J. Baker-Jarvis, M. D. Janezic, J. H. Grosvenor Jr, and R. G. Geyer, *Transmission/reflection and short-circuit line methods for measuring permittivity and permeability*. 1993.

[72] E. Handoko, A. M. Mangasi, S. Iwan, M. Randa, and M. Alaydrus, “Measurement of complex permittivity and permeability of hexagonal ferrite composite material using a waveguide in microwave band,” *Proceeding - 2016 Int. Conf. Radar, Antenna, Microwave, Electron. Telecommun. ICRAMET 2016*, pp. 28–30, 2017.

[73] G. F. Engen and C. A. Hoer, “Thru-Reflect-Line: An Improved Technique for Calibrating the Dual Six-Port Automatic Network Analyzer,” *IEEE Trans. Microw. Theory Tech.*, 1979.

[74] J. J. Martin *et al.*, “Direct-write 3D printing of composite materials with magnetically aligned discontinuous reinforcement,” vol. 10194, p. 101941I, 2017.

[75] J. J. Martin, B. E. Fiore, and R. M. Erb, “Designing bioinspired composite reinforcement architectures via 3D magnetic printing,” *Nat. Commun.*, vol. 6, pp. 1–7, 2015.

[76] L. Ren, B. Li, Z. Song, Q. Liu, L. Ren, and X. Zhou, “Bioinspired fiber-regulated composite with tunable permanent shape and shape memory properties via 3d magnetic printing,” *Compos. Part B*, vol. 164, no. December 2018, pp. 458–466, 2019.

[77] Z. Chen *et al.*, “3D Printing of Multifunctional Hydrogels,” *Adv. Funct. Mater.*, vol. 1900971, p. 1900971, 2019.

[78] H. Kim, F. Torres, D. Villagran, C. Stewart, Y. Lin, and T. L. B. Tseng, “3D Printing of BaTiO3/PVDF Composites with Electric In Situ Poling for Pressure Sensor Applications,” *Macromol. Mater. Eng.*, vol. 302, no. 11, pp. 1–6, 2017.

[79] F. Castles *et al.*, “Microwave dielectric characterisation of 3D-printed BaTiO3/ABS polymer composites,” *Sci. Rep.*, vol. 6, no. March, pp. 1–8, 2016.

[80] S. Sato, D. Gondo, T. Wada, S. Kanehashi, and K. Nagai, “Effects of various liquid organic solvents on solvent-induced crystallization of amorphous poly(lactic acid) film,” *J. Appl. Polym. Sci.*, vol. 129, no. 3, pp. 1607–1617, 2013.

[81] P. Shepherd, K. K. Mallick, and R. J. Green, “Magnetic and structural properties of M-type barium hexaferrite prepared by co-precipitation,” *J. Magn. Magn. Mater.*, vol. 311, no. 2, pp. 683–692, 2007.